

The Extended *Chandra* Deep Field-South Survey. *Chandra* Point-Source Catalogs

B. D. Lehmer,¹ W. N. Brandt,¹ D. M. Alexander,² F. E. Bauer,³ D. P. Schneider,¹ P. Tozzi,⁴ J. Bergeron,⁵
 G. P. Garmire,¹ R. Giacconi,⁶ R. Gilli,⁷ G. Hasinger,⁸ A. E. Hornschemeier,^{9,6} A. M. Koekemoer,¹⁰
 V. Mainieri,⁸ T. Miyaji,¹¹ M. Nonino,⁴ P. Rosati,¹² J. D. Silverman,⁸ G. Szokoly,⁸ & C. Vignali¹³

ABSTRACT

We present *Chandra* point-source catalogs for the Extended *Chandra* Deep Field-South (E-CDF-S) survey. The E-CDF-S consists of four contiguous 250 ks *Chandra* observations covering an approximately square region of total solid angle $\approx 0.3 \text{ deg}^2$, which flank the existing $\approx 1 \text{ Ms}$ *Chandra* Deep Field-South (CDF-S). The survey reaches sensitivity limits of $\approx 1.1 \times 10^{-16} \text{ erg cm}^{-2} \text{ s}^{-1}$ and $\approx 6.7 \times 10^{-16} \text{ erg cm}^{-2} \text{ s}^{-1}$ for the 0.5–2.0 keV and 2–8 keV bands, respectively. We detect 762 distinct X-ray point sources within the E-CDF-S exposure; 589 of these sources are new (i.e., not previously detected in the $\approx 1 \text{ Ms}$ CDF-S). This brings the total number of X-ray point sources detected in the E-CDF-S region to 915 (via the E-CDF-S and $\approx 1 \text{ Ms}$ CDF-S observations). Source positions are determined using matched-filter and centroiding techniques; the median positional uncertainty is $\approx 0''.35$. The basic X-ray and optical properties of these sources indicate a variety of source types, although absorbed active galactic nuclei (AGNs) seem to dominate. In addition to our main *Chandra* catalog, we constructed a supplementary source catalog containing 33 lower significance X-ray point sources that have bright optical counterparts ($R < 23$). These sources generally have X-ray-to-optical

¹Department of Astronomy & Astrophysics, 525 Davey Lab, The Pennsylvania State University, University Park, PA 16802, USA

²Institute of Astronomy, Madingley Road, Cambridge, CB3 0HA, United Kingdom

³Columbia Astrophysics Laboratory, Columbia University, Pupin Laboratories, 550 W. 120th St., Rm 1418, New York, NY 10027, USA

⁴INAF - Osservatorio Astronomico di Trieste, via G. B. Tiepolo 11, 34131 Trieste, Italy

⁵Institut d'Astrophysique de Paris, 98bis Boulevard, F-75014 Paris, France

⁶Department of Physics and Astronomy, Johns Hopkins University, 3400 North Charles Street, Baltimore, MD 21218, USA

⁷Istituto Nazionale di Astrofisica (INAF) - Osservatorio Astrofisico di Arcetri, Largo E. Fermi 5, 50125 Firenze, Italy

⁸Max-Planck-Institut für extraterrestrische Physik, Giessenbachstrasse, D-85748 Garching b. München, Germany

⁹Laboratory for X-ray Astrophysics, NASA Goddard Space Flight Center, Code 662, Greenbelt, MD 20771, USA

¹⁰Space Telescope Science Institute, 3700 San Martin Drive, Baltimore, MD 21218, USA

¹¹Department of Physics, Carnegie Mellon University, Pittsburgh, PA 15213, USA

¹²European Southern Observatory, Karl-Schwarzschild-Strasse 2, Garching, D-85748, Germany

¹³Dipartimento di Astronomia, Università degli Studi di Bologna, Via Ranzani 1, 40127 Bologna, Italy

flux ratios expected for normal and starburst galaxies, which lack a strong AGN component. We present basic number-count results for our main *Chandra* catalog and find good agreement with the ≈ 1 Ms CDF-S for sources with 0.5–2.0 keV and 2–8 keV fluxes greater than 3×10^{-16} erg cm $^{-2}$ s $^{-1}$ and 1×10^{-15} erg cm $^{-2}$ s $^{-1}$, respectively. Furthermore, three extended sources are detected in the 0.5–2.0 keV band, which are found to be likely associated with galaxy groups or poor clusters at $z \approx 0.1$ –0.7; these have typical rest-frame 0.5–2.0 keV luminosities of $(1\text{--}5) \times 10^{42}$ erg s $^{-1}$.

Subject headings: cosmology: observations — diffuse radiation — galaxies:active — surveys — X-rays

1. Introduction

Deep and wide X-ray surveys indicate that the cosmic X-ray background is largely due to accretion onto supermassive black holes (SMBHs) integrated over cosmic time (e.g., see Brandt & Hasinger 2005 for a review). Follow-up studies of deep-survey sources with 8–10 m optical telescopes as well as multi-wavelength correlative studies have shown that most of the X-ray sources are active galactic nuclei (AGNs), many of which are obscured (e.g., Bauer et al. 2004; Szokoly et al. 2004; Barger et al. 2005). X-ray surveys have found the highest density of AGNs on the sky (up to ≈ 7200 deg $^{-2}$). In addition to AGNs, the deepest X-ray surveys have also detected respectable numbers of starburst and normal galaxies out to cosmologically interesting distances ($z \approx 1$; e.g., Hornschemeier et al. 2003; Bauer et al. 2004; Norman et al. 2004).

Presently, the two deepest X-ray surveys are the ≈ 2 Ms *Chandra* Deep Field-North (CDF-N; Brandt et al. 2001, hereafter B01; Alexander et al. 2003, hereafter A03) and the ≈ 1 Ms *Chandra* Deep Field-South (CDF-S; Giacconi et al. 2002, hereafter G02). These ≈ 400 arcmin 2 surveys have been performed in regions of sky with extensive multiwavelength coverage. They have provided 50–250 times the sensitivity of surveys by previous X-ray missions, detecting large numbers of point sources (584 for the CDF-N and 346 for the CDF-S; G02; A03) and about a dozen extended groups and poor clusters (Bauer et al. 2002; G02).

The X-ray surveys performed to date have explored an impressive amount of the sensitivity versus solid angle “discovery space” (see Figure 1 and Brandt & Hasinger 2005). However, one limitation of the present surveys is that there is only a relatively small amount of sky probed to 0.5–2 keV flux levels of $(2\text{--}50) \times 10^{-17}$ erg cm $^{-2}$ s $^{-1}$, a flux regime where many obscured AGNs are observed (e.g., Bauer et al. 2004). As a result, our understanding of the X-ray universe at these faint fluxes suffers from limited source statistics and field-to-field variance. To mitigate this limitation, the Extended *Chandra* Deep Field-South (E-CDF-S) survey was undertaken as part of the *Chandra* Cycle 5 guest observer program. The E-CDF-S is composed of four 250 ks *Chandra* ACIS-I pointings flanking the original CDF-S; these are arranged in a contiguous two-by-two pattern and cover a total solid angle of ≈ 1100 arcmin 2 .¹

¹The ≈ 1 Ms CDF-S data cover $\approx 35\%$ of the E-CDF-S; much of this coverage, however, has limited sensitivity due to point

The pointings have sufficient sensitivity to detect the X-ray emission from moderate-luminosity AGNs ($L_X = 10^{43}$ – 10^{44} erg s $^{-1}$) to $z \approx 3$ – 6 as well as X-ray luminous starburst galaxies to $z \approx 1$. The E-CDF-S therefore can significantly improve understanding of SMBH accretion at high redshift where the source statistics are still limited. The contiguous nature of the E-CDF-S will allow wider field studies of the remarkable AGN clustering already found in the CDF-S (e.g., Gilli et al. 2003, 2005), and comparisons with other surveys of comparable depth (e.g., Stern et al. 2002; Harrison et al. 2003; Wang et al. 2004a,b; Nandra et al. 2005) will allow further assessment of the field-to-field variance of X-ray source populations.

The E-CDF-S field was selected for this program primarily due to its superb and growing multiwavelength coverage over a ≈ 900 arcmin 2 area, which ensures that it will remain a prime survey field in coming decades (see Figure 2). For example, the E-CDF-S has been imaged intensively with the *HST* Advanced Camera for Surveys (ACS) via the Galaxy Evolution from Morphology and Spectral Energy Distributions (GEMS; Rix et al. 2004; 117 *HST* orbits) and Great Observatories Origins Deep Survey (GOODS; Giavalisco et al. 2004; 199 *HST* orbits) projects. Excellent ground-based imaging is also available (e.g., Arnouts et al. 2001; Renzini et al. 2003; Giavalisco et al. 2004; Wolf et al. 2004; Gawiser et al. 2005), and several spectroscopic campaigns are underway to identify sources in the E-CDF-S, most notably with the Very Large Telescope (VLT; e.g., Le Fevre et al. 2004; Szokoly et al. 2004; Vanzella et al. 2005). The E-CDF-S has been targeted by *Spitzer* via the GOODS (M. Dickinson et al., in preparation), the *Spitzer* Wide-Area Infrared Extragalactic Survey (SWIRE; Lonsdale et al. 2003), guaranteed time (e.g., Papovich et al. 2004), and guest observer (PI: P. van Dokkum) programs. Radio observations of the E-CDF-S have been made with the Australia Telescope Compact Array (ATCA; J. Afonso et al., in preparation) and the Very Large Array.

In this paper, we present *Chandra* point-source catalogs and data products derived from the E-CDF-S data set along with details of the observations, data reduction, and technical analysis. The observational procedures and data processing were similar in nature to those presented in B01 and A03. Detailed follow-up investigations and scientific interpretation of the E-CDF-S sources will be presented in subsequent papers.

The Galactic column density along the line of sight to the E-CDF-S is remarkably low: $N_H = 8.8 \times 10^{19}$ cm $^{-2}$ (e.g., Stark et al. 1992). The coordinates throughout this paper are J2000. Cosmological parameters of $H_0 = 70$ km s $^{-1}$ Mpc $^{-1}$, $\Omega_M = 0.3$, and $\Omega_\Lambda = 0.7$ are adopted.

spread function (PSF) broadening and vignetting at large off-axis angles (see § 3 for details). The same effects limit the sensitivity and positions derived from the *XMM-Newton* data (Streblyanska et al. 2004) extending outside the region with *Chandra* coverage.

2. Observations and Data Reduction

2.1. Instrumentation and Observations

The Advanced CCD Imaging Spectrometer (ACIS; Garmire et al. 2003) was used for all of the *Chandra* observations.² ACIS is composed of ten CCDs (each 1024×1024 pixels) designed for efficient X-ray source detection and spectroscopy. ACIS-I consists of four CCDs (CCDs I0–I3) arranged in a 2×2 array with each CCD tipped slightly to approximate the curved focal surface of the *Chandra* High Resolution Mirror Assembly (HRMA). The aim-point of ACIS-I lies on CCD I3. The remaining six CCDs (ACIS-S; CCDs S0–S5) reside in a linear array and are tipped to approximate the Rowland circle of the objective gratings that can be inserted behind the HRMA.

The ACIS-I full field of view is $16'9 \times 16'9$ (≈ 285 arcmin²), and the sky-projected ACIS pixel size is $\approx 0''.492$. The PSF is smallest at the lowest photon energies and for sources at small off-axis angles. For example, the 95% encircled-energy radius at 1.5 keV for off-axis angles of $0'–8'$ is $\approx 1''.8–7''.5$ (Feigelson, Broos, & Gaffney 2000; Jerius et al. 2000).³ The PSF is approximately circular at small off-axis angles, broadens and elongates at intermediate off-axis angles, and becomes complex at large off-axis angles.

The entire *Chandra* observation program consisted of nine separate *Chandra* observations taken between 2004 February 29 and 2004 November 20 and is described in Table 1. The four ACIS-I CCDs were operated in all of the observations; the ACIS-S CCD S2 was in operation for observations 5019–5022 and 6164. Due to the large off-axis angle of ACIS-S, and consequently its low sensitivity, these data were not used in this analysis. All observations were taken in Very Faint mode to improve the screening of background events and thus increase the sensitivity of ACIS in detecting faint X-ray sources.⁴ The observations were made in four distinct observational fields (hereafter, fields 1, 2, 3, and 4; see Table 1 for more observational details) and cover a total solid angle of 1128.4 arcmin². The focal-plane temperature was kept at $\approx -120^\circ$ C for all of the nine observations.

Background light curves for all nine observations were inspected using EVENT BROWSER in the Tools for ACIS Real-time Analysis (TARA; Broos et al. 2000) software package.⁵ All but two are free from significant flaring and are stable to within $\approx 20\%$. The two observations with significant flaring are 5015 and 5017. The background was $\gtrsim 1.5$ times higher than nominal for two ≈ 1 ks intervals of observation 5015, and during observation 5017 the background rose to $\gtrsim 1.5$ times the nominal rate and remained above this level for ≈ 10 ks near the end of the observation. Intervals with flaring were retained because the flaring strengths were not strong enough to have significant negative effects on our analyses.

²For additional information on ACIS and *Chandra* see the *Chandra* Proposers' Observatory Guide at <http://cxc.harvard.edu/proposer/CfP/>.

³Feigelson et al. (2000) is available at <http://www.astro.psu.edu/xray/acis/memos/memoindex.html>.

⁴For more information on the Very Faint mode see http://cxc.harvard.edu/cal/Acis/Cal_prods/vfbkgrnd/ and Vikhlinin (2001).

⁵TARA is available at <http://www.astro.psu.edu/xray/docs>.

2.2. Data Reduction

Chandra X-ray Center (hereafter CXC) pipeline software was used for basic data processing, and the pipeline versions are listed in Table 1. The reduction and analysis of the data used *Chandra* Interactive Analysis of Observations (CIAO) Version 3.2 tools whenever possible;⁶ however, custom software, including the TARA package, was also used extensively.

All data were corrected for the radiation damage sustained by the CCDs during the first few months of *Chandra* operations using the Charge Transfer Inefficiency (CTI) correction procedure of Townsley et al. (2000, 2002).⁷ In addition to correcting partially for the positionally dependent grade distribution due to CTI effects, this procedure also partially corrects for quantum efficiency losses (see Townsley et al. 2000, 2002 for further details).

All bad columns, bad pixels, and cosmic ray afterglows were removed using the “status” information in the event files, and we only used data taken during times within the CXC-generated good-time intervals. The CIAO tool ACIS_PROCESS_EVENTS was used to remove the standard pixel randomization.

3. Production of the Point-Source Catalogs

By design, the four 250 ks E-CDF-S observations have their regions of highest sensitivity located where the sensitivity of the original ≈ 1 Ms CDF-S observation is poorest (see Table 1 and Figures 2 and 17). The loss of sensitivity is due to the combination of substantial degradation of the *Chandra* PSF at large off-axis angles and vignetting. In fact, most of the area where the E-CDF-S observations have their highest sensitivity lack any *Chandra* coverage in the ≈ 1 Ms CDF-S. We experimented with source searching utilizing the addition of the ≈ 1 Ms CDF-S and the 250 ks E-CDF-S images; such searching was done with WAVDETECT (Freeman et al. 2002) runs that did not utilize detector-specific PSF information (i.e., the “DETNAME” keyword in the image files was deleted). However, such searching did not find a substantial number of new sources compared to those presented below combined with those from the original ≈ 1 Ms CDF-S (G02; A03); these results were verified via inspection of adaptively smoothed images. Therefore, our basic approach here is to present just the sources detected in the new 250 ks E-CDF-S observations. The X-ray sources in the ≈ 1 Ms CDF-S catalog of A03 were processed using the same techniques presented here with two main differences:

1. Our main *Chandra* catalog includes sources detected by running WAVDETECT at a false-positive probability threshold of 10^{-6} , somewhat less conservative than the 10^{-7} value adopted by A03; see § 3.2 for details.

⁶See <http://cxc.harvard.edu/ciao/> for details on CIAO.

⁷The software associated with the correction method of Townsley et al. (2000, 2002) is available at <http://www.astro.psu.edu/users/townsley/cti/>.

2. The E-CDF-S consists of four ACIS-I observational fields and subtends a larger solid angle than the fields presented in A03. Therefore, our main *Chandra* catalog of the entire E-CDF-S exposure was generated by merging sub-catalogs created in each of the four observational fields; see § 3.2, Table 1, and Figure 2 for details.

3.1. Image and Exposure-Map Creation

We constructed images of each of the four E-CDF-S fields using the standard *ASCA* grade set (*ASCA* grades 0, 2, 3, 4, 6) for three standard bands (i.e., 12 images in total): 0.5–8.0 keV (full band; FB), 0.5–2.0 keV (soft band; SB), and 2–8 keV (hard band; HB). These images have $0''.492$ per pixel. For each of the standard bands, the images from all four observational fields were merged into a single image using the CIAO script `MERGE_ALL`.⁸ In Figures 3 and 4 we display the full-band raw and exposure-corrected adaptively smoothed images (see discussion below), respectively.⁹ Our point-source detection analyses have been restricted to the raw images constructed for each of the four observational fields so that the *Chandra* PSF is accounted for correctly (see § 3.2).

We constructed exposure maps for each of the four observational fields in the three standard bands. These were created following the basic procedure outlined in § 3.2 of Hornschemeier et al. (2001) and are normalized to the effective exposures of sources located at the aim points. Briefly, this procedure takes into account the effects of vignetting, gaps between the CCDs, bad column filtering, and bad pixel filtering. Also, with the release of CIAO version 3.2, the spatially dependent degradation in quantum efficiency due to contamination on the ACIS optical blocking filters is now incorporated into the generation of exposure maps.¹⁰ A photon index of $\Gamma = 1.4$, the slope of the X-ray background in the 0.5–8.0 keV band (e.g., Marshall et al. 1980; Gendreau et al. 1995), was assumed in creating the exposure maps. For each standard band, a total exposure map, covering the entire E-CDF-S, was constructed by merging the exposure maps of the four observational fields using the CIAO script `DMREGRID`. The resulting full-band exposure map is shown in Figure 5. Figure 6 displays the survey solid angle as a function of full-band effective exposure for both the total E-CDF-S exposure (Figure 6a) and the four individual observational fields (Figure 6b). Each observational field has comparable coverage with the majority of the solid angle coverage (≈ 900 arcmin²) having at least 200 ks of effective exposure.

Using the exposure maps and adaptively smoothed images discussed above, we produced exposure-corrected images following the prescription outlined in § 3.3 of Baganoff et al. (2003). Figure 7 shows a “false-color” composite image made using exposure-corrected adaptively smoothed 0.5–2.0 keV (red),

⁸See http://cxc.harvard.edu/ciao/threads/merge_all/

⁹Raw and adaptively smoothed images for all three standard bands are available at the E-CDF-S website (see <http://www.astro.psu.edu/users/niel/ecdfs/ecdfs-chandra.html>). Furthermore, equivalent images obtained by merging the E-CDF-S and CDF-S are also available at the E-CDF-S website.

¹⁰See <http://cxc.harvard.edu/ciao/why/acisqedeg.html>

2–4 keV (green), and 4–8 keV (blue) images.

3.2. Point-Source Detection

Point-source detection was performed in each band with WAVDETECT using a “ $\sqrt{2}$ sequence” of wavelet scales (i.e., 1, $\sqrt{2}$, 2, $2\sqrt{2}$, 4, $4\sqrt{2}$, and 8 pixels). Our key criterion for source detection, and inclusion in the main *Chandra* catalog, is that a source must be found with a given false-positive probability threshold in at least one of the three standard bands. The false-positive probability threshold in each band was set to 1×10^{-6} ; a total of 762 distinct sources met this criterion. We also ran WAVDETECT using false-positive probability thresholds of 1×10^{-7} and 1×10^{-8} to evaluate the significance of each detected source.

If we conservatively treat the 12 images (i.e., the three standard bands over the four observational fields) as being independent, it appears that ≈ 50 (i.e., $\approx 6\%$) false sources are expected in our total *Chandra* source catalog for the case of a uniform background over $\approx 5.0 \times 10^7$ pixels. However, since WAVDETECT suppresses fluctuations on scales smaller than the PSF, a single pixel usually should not be considered a source detection cell, particularly at large off-axis angles. Hence, our false-source estimates are conservative. As quantified in § 3.4.1 of A03 and by new source-detection simulations (P. E. Freeman 2005, private communication), the number of false-sources is likely ≈ 2 – 3 times less than our conservative estimate, leaving only ≈ 15 – 25 (i.e., $\lesssim 3\%$) false sources. In § 3.3.1 below we provide additional source-significance information that a user can utilize to perform more conservative source screening if desired.

3.3. Point-Source Catalogs

3.3.1. Main *Chandra* Source Catalog

We ran WAVDETECT with a false-positive probability threshold of 1×10^{-6} on all of the 12 images. The resulting source lists were then merged to create the point-source catalog given in Table 2. For cross-band matching, a matching radius of $2''.5$ was used for sources within $6'$ of the average aim point. For larger off-axis angles, a matching radius of $4''.0$ was used. These matching radii were chosen based on inspection of histograms showing the number of matches obtained as a function of angular separation (e.g., see §2 of Boller et al. 1998); with these radii the mismatch probability is $\lesssim 1\%$ over the entire field.

We improved the WAVDETECT source positions using a matched-filter technique (A03). This technique convolves the full-band image in the vicinity of each source with a combined PSF. The combined PSF is automatically generated as part of the ACIS_EXTRACT procedure (Broos et al. 2002) within TARA (see Footnote 5) and is produced by combining the “library” PSF of a source for each observation, weighted by the number of detected counts.¹¹ This technique takes into account the fact that, due to the complex PSF

¹¹ACIS_EXTRACT can be accessed from http://www.astro.psu.edu/xray/docs/TARA/ae_users_guide.html. The PSFs are taken

at large off-axis angles, the X-ray source position is not always located at the peak of the X-ray emission. The matched-filter technique provides a small improvement ($\approx 0''.1$ on average) in the positional accuracy for sources further than $6'$ from the average aim-point. For sources with off-axis angles (θ) $< 6'$, we found that the off-axis-angle-weighted combination of centroid and matched-filter positions returned the most significant improvement to source positions. Algebraically, this can be written as:

$$(6' - \theta)/6' \times \text{centroid position} + \theta/6' \times \text{matched-filter position} \quad (1)$$

This method is similar to that employed by A03.

Manual correction of the source properties was required in some special cases: (1) There were 11 close doubles (i.e., sources with overlapping PSFs) and one close triple. These sources incur large photometric errors due to the difficulty of the separation process. (2) A total of eight sources were located close to bright sources, in regions of high background, in regions with strong gradients in exposure time, or partially outside of an observational field. The properties of these sources have been adjusted manually and are flagged in column 39 of Table 2 (see below).

For each observational field, we refined the absolute X-ray source positions by matching X-ray sources from the main point-source catalog to R -band optical source positions from deep observations ($R_{\text{lim},6\sigma} \approx 27$ [AB] over the entire E-CDF-S) obtained with the Wide Field Imager (WFI) of the MPG/ESO telescope at LaSilla (see § 2 of Giavalisco et al. 2004). X-ray sources from each of the four observational fields were matched to optical sources using a $2''.5$ matching radius. Using this matching radius, a small number of sources were observed to have more than one optical match; the brightest of these sources was selected as the most probable counterpart. Under these criteria, 640 ($\approx 84\%$) X-ray sources have optical counterparts. We also note that in a small number of cases the X-ray source may be offset from the center of the optical source even though both are associated with the same galaxy (e.g., a galaxy with bright optical emission from starlight that also has an off-nuclear ultraluminous X-ray binary with $L_X \approx 10^{38-40}$ erg s $^{-1}$; see e.g., Hornschemeier et al. 2004). The accuracy of the X-ray source positions was improved by centering the distribution of offsets in right ascension and declination between the optical and X-ray source positions; this resulted in small ($< 1''.0$) field-dependent astrometric shifts for all sources in each field. We also checked for systematic offsets as a function of right ascension and declination that may arise from differing “plate scales” and rotations between the X-ray and optical images. These investigations were performed by plotting the right ascension and declination offsets (between optical and X-ray sources) as functions of right ascension and declination; no obvious systematic offsets were found.

Figure 8 shows the positional offset between the X-ray and optical sources versus off-axis angle after applying the positional corrections discussed above. Here, the off-axis angles are computed for each observational field appropriately; this allows for the consistent analysis of *Chandra* positional uncertainties as a function of off-axis angle. The median offset is $\approx 0''.35$; however, there are clear off-axis angle and

from the CXC PSF library; see <http://cxc.harvard.edu/ciao/dictionary/psflib.html>.

source-count dependencies. The off-axis angle dependence is due to the HRMA PSF becoming broad at large off-axis angles, while the count dependency is due to the difficulty of centroiding a faint X-ray source. The median offset of the bright X-ray sources (≥ 50 full-band counts) is only $\approx 0''.25$, while the median offset of the faint X-ray sources (< 50 full-band counts) is $\approx 0''.47$. The positional uncertainty of each source is estimated following equations 2 and 3.

The main *Chandra* source catalog is presented in Table 2, and the details of the columns are given below.

- Column 1 gives the source number. Sources are listed in order of increasing RA.
- Columns 2 and 3 give the RA and Dec of the X-ray source, respectively. Note that more accurate positions are available for sources detected near the aim-point of the ≈ 1 Ms CDF-S through the catalogs presented in A03; see columns 19–21. To avoid truncation error, we quote the positions to higher precision than in the International Astronomical Union (IAU) registered names beginning with the acronym “CXO ECDFS” for “*Chandra* X-ray Observatory Extended *Chandra* Deep Field-South.” The IAU names should be truncated after the tenths of seconds in RA and after the arcseconds in Dec.
- Column 4 gives the positional uncertainty. As shown above, the positional uncertainty is dependent on off-axis angle and the number of detected counts. For the brighter X-ray sources (≥ 50 full-band counts) the positional uncertainties are given by the empirically determined equation:

$$\Delta = \begin{cases} 0.6 & \theta < 5' \\ 0.6 + \left(\frac{\theta - 5'}{20'}\right) & \theta \geq 5' \end{cases} \quad (2)$$

where Δ is the positional uncertainty in arcseconds and θ is the off-axis angle in arcminutes (compare with Figure 8).

For the fainter X-ray sources (< 50 full-band counts) the positional uncertainties are given by the empirically determined equation:

$$\Delta = \begin{cases} 0.85 & \theta < 5' \\ 0.85 + \left(\frac{\theta - 5'}{4'}\right) & \theta \geq 5' \end{cases} \quad (3)$$

The stated positional uncertainties are somewhat conservative, corresponding to the ≈ 80 – 90% confidence level.

- Column 5 gives the off-axis angle for each source in arcminutes. This is calculated using the source position given in columns 2 and 3 and the aim point (see Table 1) for the corresponding field in which it was detected (column 37).

- Columns 6–14 give the source counts and the corresponding 1σ upper and lower statistical errors (from Gehrels 1986), respectively, for the three standard bands. All values are for the standard *ASCA* grade set, and they have not been corrected for vignetting. Source counts and statistical errors have been calculated using circular aperture photometry; extensive testing has shown that this method is more reliable than the *WAVDETECT* photometry. The circular aperture was centered at the position given in columns 2 and 3 for all bands.

The local background is determined in an annulus outside of the source-extraction region. The mean number of background counts per pixel is calculated from a Poisson model using $\frac{n_1}{n_0}$, where n_0 is the number of pixels with 0 counts and n_1 is the number of pixels with 1 count. Although only the numbers of pixels with 0 and 1 counts are measured, this technique directly provides the mean background even when $n_1 \gg n_0$. Furthermore, by ignoring all pixels with more than 1 count, this technique guards against background contamination from sources. We note that relatively bright nearby sources may contribute counts to nearby pixels where the background is estimated. Since the number density of relatively bright sources in the E-CDF-S is low, we estimate that only ≈ 10 – 20 of these sources are thereby contaminated; the majority of these sources have been corrected via manual photometry of close doubles (see above). The principal requirement for using this Poisson-model technique is that the background is low and follows a Poisson distribution; in §4.2 of A03 it has been shown that the *ACIS-I* background matches this criterion for exposures as long as ≈ 2 Ms. The total background for each source is calculated and subtracted to give the net number of source counts.

For sources with fewer than 1000 full-band counts, we have chosen the aperture radii based on the encircled-energy function of the *Chandra* PSF as determined using the CXC’s *MKPSF* software (Feigelson et al. 2000; Jerius et al. 2000). In the soft band, where the background is lowest, the aperture radius was set to the 95% encircled-energy radius of the PSF. In the other bands, the 90% encircled-energy radius of the PSF was used. Appropriate aperture corrections were applied to the source counts by dividing the extracted source counts by the encircled-energy fraction for which the counts were extracted.

For sources with more than 1000 full-band counts, systematic errors in the aperture corrections often exceed the expected errors from photon statistics when the apertures described in the previous paragraph are used. Therefore, for such sources we used larger apertures to minimize the importance of the aperture corrections; this is appropriate since these bright sources dominate over the background. We set the aperture radii to be twice those used in the previous paragraph and inspected these sources to verify that the measurements were not contaminated by neighboring objects.

We have performed several consistency tests to verify the quality of the photometry. For example, we have checked that the sum of the counts measured in the soft and hard bands does not differ from the counts measured in the full band by an amount larger than that expected from measurement error. Systematic errors that arise from differing full-band counts and soft-band plus hard-band counts are estimated to be $\lesssim 4\%$.

When a source is not detected in a given band, an upper limit is calculated; upper limits are indicated as a “–1” in the error columns. All upper limits are determined using the circular apertures described

above. When the number of counts in the aperture is ≤ 10 , the upper limit is calculated using the Bayesian method of Kraft, Burrows, & Nousek (1991) for 99% confidence. The uniform prior used by these authors results in fairly conservative upper limits (see Bickel 1992), and other reasonable choices of priors do not materially change our scientific results. For larger numbers of counts in the aperture, upper limits are calculated at the 3σ level for Gaussian statistics.

- Columns 15 and 16 give the RA and Dec of the optical source centroid, which was obtained by matching our X-ray source positions (columns 2 and 3) to WFI *R*-band positions using a matching radius of 1.5 times the positional uncertainty quoted in column 4. For a small number of sources more than one optical match was found, and for these sources the brightest match was selected as the most probable counterpart. Using these criteria, 594 ($\approx 78\%$) of the sources have optical counterparts. Note that the matching criterion used here is more conservative than that used in the derivation of our positional errors discussed in § 3.3.1. Sources with no optical counterparts have RA and Dec values set to “00 00 00.00” and “+00 00 00.0”.
- Column 17 gives the measured offset between the optical and X-ray sources (i.e., $O-X$) in arcseconds. Sources with no optical counterparts have a value set to “0”.
- Column 18 gives the *R*-band magnitude (AB) of each X-ray source. Sources with no optical counterparts have a value set to “0”.
- Column 19 gives the ≈ 1 Ms CDF-S source number from the main *Chandra* catalog presented in A03 (see column 1 of Table 3a in A03) for E-CDF-S sources that were matched to A03 counterparts. We used a matching radius of 1.5 times the sum of the positional errors of the E-CDF-S and A03 source positions. We note that for each matched source only one match was observed; E-CDF-S sources with no A03 match have a value of “0”.
- Columns 20 and 21 give the RA and Dec of the corresponding ≈ 1 Ms CDF-S A03 source indicated in column 19. Sources with no A03 match have RA and Dec values set to “00 00 00.00” and “+00 00 00.0”.
- Column 22 gives the ≈ 1 Ms CDF-S source number from the main *Chandra* catalog presented in G02 (see “ID” column of Table 2 in G02) for E-CDF-S sources that were matched to G02 counterparts. When matching our E-CDF-S source positions with G02 counterparts, we removed noted offsets to the G02 positions of $-1''.2$ in RA and $+0''.8$ in Dec (see § A3 of A03); these positions are corrected in the quoted source positions in columns 23 and 24. We used a matching radius of 1.5 times the E-CDF-S positional error plus the G02-quoted positional error for each source position. We note that for each matched source only one match was observed; E-CDF-S sources with no G02 match have a value of “0”.
- Columns 23 and 24 give the RA and Dec of the corresponding ≈ 1 Ms CDF-S G02 source indicated in column 22. Note that the quoted positions have been corrected by the noted offsets described in column 22 (see § A3 of A03). Sources with no G02 match have RA and Dec values set to “00 00 00.00” and “+00 00 00.0”.

- Columns 25–27 give the effective exposure times derived from the standard-band exposure maps (see §3.1 for details on the exposure maps). Dividing the counts listed in columns 6–14 by the corresponding effective exposures will provide vignetting-corrected and quantum efficiency degradation-corrected count rates.
- Columns 28–30 give the band ratio, defined as the ratio of counts between the hard and soft bands, and the corresponding upper and lower errors, respectively. Quoted band ratios have been corrected for differential vignetting between the hard band and soft band using the appropriate exposure maps. Errors for this quantity are calculated following the “numerical method” described in §1.7.3 of Lyons (1991); this avoids the failure of the standard approximate variance formula when the number of counts is small (see §2.4.5 of Eadie et al. 1971). Note that the error distribution is not Gaussian when the number of counts is small. Upper limits are calculated for sources detected in the soft band but not the hard band and lower limits are calculated for sources detected in the hard band but not the soft band. For these sources, the upper and lower errors are set to the computed band ratio.
- Columns 31–33 give the effective photon index (Γ) with upper and lower errors, respectively, for a power-law model with the Galactic column density. The effective photon index has been calculated based on the band ratio in column 28 when the number of counts is not low.

A source with a low number of counts is defined as being (1) detected in the soft band with < 30 counts and not detected in the hard band, (2) detected in the hard band with < 15 counts and not detected in the soft band, (3) detected in both the soft and hard bands, but with < 15 counts in each, or (4) detected only in the full band. When the number of counts is low, the photon index is poorly constrained and is set to $\Gamma = 1.4$, a representative value for faint sources that should give reasonable fluxes. Upper and lower limits are indicated by setting the upper and lower errors to the computed effective photon index.

- Columns 34–36 give observed-frame fluxes in the three standard bands; quoted fluxes are in units of 10^{-15} erg cm $^{-2}$ s $^{-1}$. Fluxes have been computed using the counts in columns 6, 9, and 12, the appropriate exposure maps (columns 25–27), and the spectral slopes given in column 31. The fluxes have not been corrected for absorption by the Galaxy or material intrinsic to the source. For a power-law model with $\Gamma = 1.4$, the soft-band and hard-band Galactic absorption corrections are $\approx 2.1\%$ and $\approx 0.1\%$, respectively. More accurate fluxes for these sources would require direct fitting of the X-ray spectra for each observation, which is beyond the scope of this paper.
- Column 37 gives the observational field number corresponding to the detected source. The observational fields overlap in a few areas (see Figures 5 and 6a) over ≈ 50 arcmin 2 , which allowed for duplicate detections of a single source. Fourteen sources in the *Chandra* catalog were detected in more than one observational field; these sources are flagged in column 39 (see below). The data from the observation that produced the greatest number of full-band counts for these sources is included here; properties derived from the cross-field observations are provided in Table 3.
- Column 38 gives the logarithm of the minimum false-positive probability run with WAVDETECT in which each source was detected (see § 3.2). A lower false-positive probability indicates a more sig-

nificant source detection. Note that 655 ($\approx 86\%$) and 596 ($\approx 78\%$) of our sources are detected with false-positive probability thresholds of 1×10^{-7} and 1×10^{-8} , respectively.

- Column 39 gives notes on the sources. “D” denotes a source detected in more than one of the four observational fields. “U” denotes objects lying in the UDF (see Figure 2). “G” denotes objects that were identified as Galactic stars through the optical spectrophotometric COMBO-17 survey (Wolf et al. 2004). “O” refers to objects that have large cross-band (i.e., between the three standard bands) positional offsets ($> 2''$); all of these sources lie at off-axis angles of $> 8'$. “M” refers to sources where the photometry was performed manually. “S” refers to close-double or close-triple sources where manual separation was required. “C” refers to sources detected within the boundary of the ≈ 1 Ms CDF-S exposure that have no A03 or G02 counterparts. Several of these sources are located in low-sensitivity regions of the ≈ 1 Ms CDF-S, and a few of these sources may be variable. For further explanation of many of these notes, see the above text in this section on manual correction of the WAVDETECT results.

In Table 3 we summarize the cross-field source properties of the 14 sources detected in more than one observational field; none of these sources were detected in more than two fields. These properties were derived from the observation not included in the main *Chandra* catalog (see columns 37 and 39 of Table 2) and are included here for comparison. The columns of Table 3 are the same as those in Table 2; the source number for each source corresponds to its duplicate listed in the main *Chandra* catalog. In Table 4 we summarize the source detections in the three standard bands for each of the observational fields and the main *Chandra* catalog. In total 776 point sources are detected in one or more of the three standard bands; 14 of these sources are detected in more than one of the four observational fields (see columns 37 and 39 of Tables 2 and 3) leaving a total of 762 distinct point sources. Out of these 762 distinct point sources, we find that 173 are coincident with sources included in the main *Chandra* catalog for the ≈ 1 Ms CDF-S presented in A03 (see columns 19–24 of Table 2). For these sources, we find reasonable agreement between the derived X-ray properties presented here and in A03. A total of 589 new point sources are thus detected here, which brings the total number of E-CDF-S plus ≈ 1 Ms CDF-S sources to 915.

In Table 5 we summarize the number of sources detected in one band but not another. All but two of the detected sources are detected in either the soft or full bands. From Tables 4 and 5, the fraction of hard-band sources not detected in the soft band is $96/453 \approx 21\%$. The fraction is somewhat higher than for the *Chandra* Deep Fields, where it is $\approx 14\%$. Some of this difference is likely due to differing methods of cross-band matching (i.e., compare § 3.4.1 of A03 with our § 3.3.1). Furthermore, this fraction is physically expected to vary somewhat with sensitivity limit. We have also attempted comparisons with X-ray surveys of comparable depth (Stern et al. 2002; Harrison et al. 2003; Wang et al. 2004a,b; Nandra et al. 2005) to the E-CDF-S. Such comparisons are not entirely straightforward due to varying energy bands utilized, source-selection techniques, and source-searching methods. However, the “hard-band but not soft-band” fractions for these surveys appear plausibly consistent ($\approx 15\text{--}25\%$) with that for the E-CDF-S.

In Figure 9 we show the distributions of detected counts in the three standard bands. There are 154 sources with > 100 full-band counts, for which basic spectral analyses are possible; there are eight sources

with > 1000 full-band counts. Figure 10 shows the distribution of effective exposure time for the three standard bands. The median effective exposure times for the soft and hard bands are ≈ 216 ks and ≈ 212 ks, respectively. In Figure 11 we show the distributions of X-ray flux in the three standard bands. The X-ray fluxes in this survey span roughly four orders of magnitude with $\approx 50\%$ of the sources having soft band fluxes less than 50×10^{-17} erg cm $^{-2}$ s $^{-1}$, a flux regime that few X-ray surveys have probed with significant areal coverage.

In Figure 12 we show “postage-stamp” images from the WFI *R*-band image with adaptively-smoothed full-band contours overlaid for sources included in the main *Chandra* catalog. The wide range of X-ray source sizes observed in these images is largely due to PSF broadening with off-axis angle. In Figure 13 we plot the positions of sources detected in the main *Chandra* catalog. Sources that are also included in the A03 CDF-S source catalog are indicated as open circles, and new X-ray sources detected in this survey are indicated as filled circles; the circle sizes depend upon the most significant false-positive probability run with WAVDETECT for which each source was detected (see column 38 of Table 2). The majority of the sources lie in the vicinities of the aim points where the fields are most sensitive. In Figure 14 we show the band ratio as a function of full-band count rate for sources in the main *Chandra* catalog. This plot shows that the mean band ratio for sources detected in both the soft and hard bands hardens for fainter fluxes, a trend observed in other studies (e.g., della Ceca et al. 1999; Ueda et al. 1999; Mushotzky et al. 2000; B01; Tozzi et al. 2001; A03). This trend is due to the detection of more absorbed AGNs at low flux levels, and it has been shown that AGNs will dominate the number counts down to 0.5–2.0 keV fluxes of $\approx 1 \times 10^{-17}$ erg cm $^{-2}$ s $^{-1}$ (e.g., Bauer et al. 2004). Figure 15a shows the *R*-band magnitude versus the soft band flux for sources included in the main *Chandra* catalog. The approximate X-ray to *R*-band flux ratios for AGNs and galaxies (e.g., Maccacaro et al. 1998; Stocke et al. 1991; Hornschemeier et al. 2001; Bauer et al. 2004) are indicated with dark and light shading, respectively. The majority of the sources in this survey appear to be AGNs. Sixty-one of the sources were reliably classified as AGNs and seventeen sources have been identified as Galactic stars (see column 39 of Table 2) in the COMBO-17 survey (Wolf et al. 2004). A significant minority of the sources appear to have X-ray-to-optical flux ratios characteristic of normal or starburst galaxies.

3.3.2. Supplementary Optically Bright *Chandra* Source Catalog

The density of optically bright ($R < 23$) sources on the sky is comparatively low. Therefore, we can search for X-ray counterparts to optically bright sources at a lower X-ray significance threshold than that used in the main catalog without introducing many false sources (see §5.3 of Richards et al. 1998 for a similar technique applied at radio wavelengths). We ran WAVDETECT with a false-positive probability threshold of 1×10^{-5} on images created in the three standard bands. A basic lower significance *Chandra* catalog was produced containing 323 X-ray sources not present in the main *Chandra* source catalog.

In our matching of these lower significance *Chandra* sources to optically bright sources, we used the WFI *R*-band source catalog described in §3.3. We searched for X-ray counterparts to these optical sources

using a matching radius of $1''.3$. Based upon offset tests, as described below, we found empirically that we could match to sources as faint as $R = 23$ without introducing an unacceptable number of false matches; this R -band cutoff provides an appropriate balance between the number of detected sources and the expected number of false sources.

In total 26 optically bright X-ray sources were found via our matching. We estimated the expected number of false matches by artificially offsetting the X-ray source coordinates in RA and Dec by both $5''$ and $10''$ (using both positive and negative shifts) and then re-correlating with the optical sources. On average ≈ 3 matches were found with these tests, demonstrating that the majority of the 26 X-ray matches are real X-ray sources; only about 12% of these sources are expected to be spurious matches.

We also included seven $R < 21$ sources where the X-ray source lay $1''.3$ – $10''.0$ from the centroid of the optical source but was still within the extent of the optical emission. Using optical spectrophotometric redshift information from COMBO-17, we required that our off-nuclear sources have 0.5–2.0 keV luminosities of $\lesssim 10^{40}$ erg s^{-1} . This restriction was intended to remove obvious sources not associated with their host galaxies; this led to the removal of one candidate source (J033210.9–280230) when forming our sample of seven plausible off-nuclear X-ray sources. Of the seven selected off-nuclear sources included in the supplementary catalog, we found that six of the host galaxies have COMBO-17 redshift information available. These galaxies were found to have $z \approx 0.10$ – 0.25 and 0.5–2.0 keV luminosities in the range of $\approx 10^{39-40}$ erg s^{-1} . These derived luminosities are consistent with these sources being off-nuclear X-ray binaries or star-forming regions associated with bright host galaxies. Since these seven sources were identified in a somewhat subjective manner, it is not meaningful to determine a false-matching probability for them. These sources are indicated in column 33 of Table 6. Thus, in total, the supplementary optically bright *Chandra* source catalog contains 33 sources.

The format of Table 6 is similar to that of Table 2. Details of the columns in Table 6 are given below.

- Column 1 gives the source number (see column 1 of Table 2 for details).
- Columns 2 and 3 give the RA and Dec of the X-ray source, respectively. The WAVDETECT positions are given for these faint X-ray sources. Whenever possible, we quote the position determined in the full band; when a source is not detected in the full band we use, in order of priority, the soft-band position and then the hard-band position. The priority ordering of position choices above was designed to maximize the signal-to-noise of the data being used for positional determination.
- Column 4 gives the positional uncertainty in arcseconds. For these faint X-ray sources, the positional uncertainty is taken to be $1''.2$, the 90th percentile of the average optical-X-ray positional offsets given in column 17.
- Column 5 gives the off-axis angle for each source in arcminutes (see column 5 of Table 2 for details).
- Columns 6–14 give the counts and the corresponding 1σ upper and lower statistical errors (using Gehrels 1986), respectively, for the three standard bands. The photometry is taken directly from WAVDETECT for these faint X-ray sources.

- Columns 15 and 16 give the RA and Dec of the optical source centroid, respectively.
- Column 17 gives the measured offset between the optical and X-ray sources (i.e., $O-X$) in arcseconds.
- Column 18 gives the R -band magnitude (AB) of the optical source.
- Column 19 gives the ≈ 1 Ms CDF-S source number from the main *Chandra* catalog presented in A03 (see column 1 of Table 3a in A03) for supplementary sources that were matched to A03 counterparts. We used a matching radius of 1.5 times the sum of the positional errors of the E-CDF-S and A03 source positions. We note that for each matched source only one match was observed; supplementary sources with no A03 match have a value of “0”.
- Columns 20 and 21 give the RA and Dec of the corresponding ≈ 1 Ms CDF-S A03 source indicated in column 19. Sources with no A03 match have RA and Dec values set to “00 00 00.00” and “+00 00 00.0”.
- Column 22 gives the ≈ 1 Ms CDF-S source number from the main *Chandra* catalog presented in G02 (see “ID” column of Table 2 in G02) for supplementary sources that were matched to G02 counterparts. When matching our supplementary source positions with G02 counterparts, we removed noted offsets to the G02 positions of $-1''.2$ in RA and $+0''.8$ in Dec (see § A3 of A03); these positions are corrected in the quoted source positions in columns 23 and 24. We used a matching radius of 1.5 times the E-CDF-S positional error plus the G02-quoted positional error for each source position. We note that for each matched source only one match was observed; supplementary sources with no G02 match have a value of “0”.
- Columns 23 and 24 give the RA and Dec of the corresponding ≈ 1 Ms CDF-S G02 source indicated in column 22. Note that the quoted positions have been corrected by the noted offsets described in column 22 (see § A3 of A03). Sources with no G02 match have RA and Dec values set to “00 00 00.00” and “+00 00 00.0”.
- Columns 25–27 give the effective exposure times derived from the standard-band exposure maps (see columns 25–27 of Table 2 for details).
- Column 28 gives the photon index used to calculate source fluxes (columns 26–28). We used a constant photon index of $\Gamma = 2.0$ since our source-selection technique preferentially selects objects with flux-ratios $f_{0.5-2.0 \text{ keV}}/f_R < 0.1$, which are observed to have effective photon indices of $\Gamma \approx 2$ (e.g., § 4.1.1 of Bauer et al. 2004).
- Column 29–31 give observed-frame fluxes in the three standard bands; quoted fluxes are in units of $10^{-15} \text{ erg cm}^{-2} \text{ s}^{-1}$ and have been calculated assuming $\Gamma = 2.0$. The fluxes have not been corrected for absorption by the Galaxy or material intrinsic to the sources (see columns 34–36 of Table 2 for details).
- Column 32 gives the observational field number corresponding to the detected source (see column 37 of Table 2 for details).

- Column 33 gives notes on the sources. With the exception of the additional note given below, the key for these notes is given in column 39 of Table 2. “L” refers to objects where the X-ray source lies $> 1''.3$ from the centroid of the optical source but is still within the extent of the optical emission (see the text above for further discussion).

The R -band magnitudes of the supplementary sources span $R = 16.6$ – 22.9 . In Figure 15b we show the R -band magnitude versus soft-band flux. All of the sources lie in the region expected for starburst and normal galaxies. Three of these sources have been classified as Galactic stars via optical classifications from COMBO-17 (see column 33 of Table 6). Some of these sources may be low-luminosity AGNs; the small number of hard-band detections ($\approx 6\%$) indicates that few of these are absorbed AGNs. Due to the low number of counts detected for these sources, we do not provide postage-stamp images as we did for sources in the main catalog (i.e., Figure 12).

The addition of the optically bright supplementary sources increases the number of extragalactic objects in the E-CDF-S with $f_{0.5-2.0 \text{ keV}}/f_R < 0.1$ and $f_{0.5-2.0 \text{ keV}}/f_R < 0.01$ by $\approx 20\%$ and $\approx 50\%$, respectively. However, the optically bright supplementary sources are not representative of the faintest X-ray sources as a whole since our selection criteria preferentially select optically bright and X-ray faint non-AGNs (e.g., A03; Hornschemeier et al. 2003).

4. Background and Sensitivity Analysis

The faintest sources in the main *Chandra* catalog have ≈ 4 counts (see Table 4). For a $\Gamma = 1.4$ power law with Galactic absorption, the corresponding soft-band and hard-band fluxes at the aim points are $\approx 8.9 \times 10^{-17} \text{ erg cm}^{-2} \text{ s}^{-1}$ and $\approx 4.4 \times 10^{-16} \text{ erg cm}^{-2} \text{ s}^{-1}$, respectively. This gives a measure of the ultimate sensitivity of this survey, however, these numbers are only relevant for a small region close to the aim point. To determine the sensitivity across the field it is necessary to take into account the broadening of the PSF with off-axis angle, as well as changes in the effective exposure and background rate across the field. We estimated the sensitivity across the field by employing a Poisson model, which was calibrated for sources detected in the main *Chandra* catalog. Our resulting relation is

$$\log(N) = \alpha + \beta \log(b) + \gamma [\log(b)]^2 + \delta [\log(b)]^3 \quad (4)$$

where N is the required number of source counts for detection, and b is the number of background counts in a source cell; $\alpha = 0.967$, $\beta = 0.414$, $\gamma = 0.0822$, and $\delta = 0.0051$ are fitting constants. The only component within this equation that we need to measure is the background. For the sensitivity calculations here we measured the background in a source cell using the background maps described below and assumed an aperture size of 70% of the encircled-energy radius of the PSF; the 70% encircled energy-radius was chosen as a compromise between having too few source counts and too many background counts. The total background includes contributions from the unresolved cosmic background, particle background, and instrumental background (e.g., Markevitch 2001; Markevitch et al. 2003). For our analyses we are only interested in the total

background and do not distinguish between these different components.

To create background maps for all of the twelve images, we first masked out the point sources from the main *Chandra* catalog using apertures with radii twice that of the $\approx 90\%$ PSF encircled-energy radii. The resultant images should include minimal contributions from detected point sources. They will, however, include contributions from extended sources (e.g., Bauer et al. 2002; see § 6), which will cause a slight overestimation of the measured background close to extended sources. Extensive testing of background-count distributions in all three standard bands has shown that the X-ray background follows a nearly Poisson count distribution (see § 4.2 of A03). We filled in the masked regions for each source with a local background estimate by making a probability distribution of counts using an annulus with inner and outer radii of 2 and 4 times the $\approx 90\%$ PSF encircled-energy radius, respectively. The background properties are summarized in Table 7, and the full-band background map is shown in Figure 16. The majority of the pixels have no background counts (e.g., in the full band $\approx 97\%$ of the pixels are zero) and the mean background count rates for these observations are broadly consistent with those presented in A03.

Following equation 4, we generated sensitivity maps using the background and exposure maps; we assumed a $\Gamma = 1.4$ power-law model with Galactic absorption. In Figure 17 we show the full-band sensitivity map, and in Figure 18 we show plots of flux limit versus solid angle for the full, soft, and hard bands. The ≈ 1 arcmin² regions at the aim points has average 0.5–2.0 keV and 2–8 keV sensitivity limits of $\approx 1.1 \times 10^{-16}$ erg cm⁻² s⁻¹ and $\approx 6.7 \times 10^{-16}$ erg cm⁻² s⁻¹, respectively. Since we do not filter out detected sources with our sensitivity maps, a number of sources have fluxes below these sensitivity limits (4 sources in the soft band and 17 sources in the hard band). Approximately 800 arcmin² of the field (i.e., ≈ 3 times the size of a single ACIS-I field) has a soft-band sensitivity limit of $\lesssim 3 \times 10^{-16}$ erg cm⁻² s⁻¹, well into the flux range where few X-ray surveys have probed (see Figure 1).

5. Number Counts for Main *Chandra* Catalog

We have calculated cumulative number counts, $N(> S)$, for the soft and hard bands using sources presented in our main *Chandra* catalog (see Table 2). We restricted our analyses to flux levels where we expect to be mostly complete based on our sensitivity maps and simulations performed by Bauer et al. (2004); this also helps to guard against Eddington bias at low flux levels. We empirically set our minimum flux levels to 3.0×10^{-16} erg cm⁻² s⁻¹ in the soft band and 1.2×10^{-15} erg cm⁻² s⁻¹ in the hard band, which correspond to the minimum detected fluxes for sources with $\gtrsim 15$ counts in each respective band.

Assuming completeness to the flux levels quoted above, the cumulative number of sources, $N(> S)$, brighter than a given flux, S , weighted by the appropriate aerial coverage, is

$$N(> S) = \sum_{S_i > S} \Omega_i^{-1} \quad (5)$$

where Ω_i is the maximum solid angle for which a source with measured flux, S_i , could be detected. Each

maximum solid angle was computed using the profiles presented in Figure 18. In Figure 19 we show the cumulative number counts for the main *Chandra* catalog. Number counts derived for the ≈ 1 Ms CDF-S from Rosati et al. (2002) have been plotted for comparison. The E-CDF-S number counts appear to be consistent with those from the ≈ 1 Ms CDF-S to within $\approx 1 \sigma$ over the overlapping flux ranges. We note, however, that the hard-band number counts appear to be generally elevated with respect to those from the ≈ 1 Ms CDF-S; this effect is likely a signature of field-to-field variance from the ≈ 1 Ms CDF-S where a smaller solid angle is surveyed. Even with the conservative flux constraints used in our number-counts analysis we reach source densities exceeding $\approx 2000 \text{ deg}^{-2}$; as noted in § 3.3.1, a large majority of these sources are AGNs. For comparison, the number density of COMBO-17 sources with reliable AGN identifications is $\approx 300 \text{ deg}^{-2}$ (Wolf et al. 2004).

6. Extended Sources

We searched the standard-band images for extended sources using the Voronoi Tessellation and Percolation algorithm VTPDETECT (Ebeling & Wiedenmann 1993; Dobrzycki et al. 2002). In our VTPDETECT searching, we adopted a false-positive probability threshold of 1×10^{-7} and a “coarse” parameter of 50. Following the source-detection criteria presented in Bauer et al. (2002), we further required that VTPDETECT-detected sources have (1) average VTPDETECT radii (i.e., average of the 3σ major and minor axes estimated by VTPDETECT) \geq three times the 95% encircled-energy radius of a point source at the given position and (2) visible evidence for extended emission in the adaptively smoothed, exposure-corrected images (see § 3.3.1 and Figure 4). Application of these somewhat conservative selection criteria yielded three extended X-ray sources, all of which are detected only in the soft band. The soft emission from the most significant of these three extended sources, CXOECDFS J033320.3–274836, is clearly visible as an extended red “glow” near the left-hand side of Figure 7.

The X-ray properties of these three extended sources are presented in Table 8; our analysis was limited to the soft band where we find all of our detections. The counts for extended sources were determined using manual aperture photometry; point sources were masked out using circular apertures with radii of twice the 95% encircled-energy radii (see Footnote 3). We extracted extended-source counts using elliptical apertures with sizes and orientations that most closely matched the apparent extent of X-ray emission ($> 10\%$ above the background level) as observed in the adaptively smoothed images (see Table 8). The local background was estimated using elliptical annuli with inner and outer sizes of 1 and 2.5 times those used for extracting source counts. In order to calculate properly the expected numbers of background counts in our source extraction regions, we extracted total exposure times from the source and background regions (with point sources removed) and normalized the extracted background counts to the source exposure times. That is, using the number of background counts b_m and total background exposure time T_m as measured from the elliptical annuli, we calculated the expected number of background counts b_s in a source extraction region with total exposure time T_s as being $b_s = b_m T_s / T_m$. This technique was used to account for extended emission from sources that are spatially distributed over more than one observational field, which was the case for CXOECDFS J033320.3–274836.

Figure 20 shows WFI *R*-band images of the extended sources with adaptively smoothed soft-band contours overlaid. Inspection of the spectrophotometric redshifts of optical sources (from COMBO-17) in these regions suggests that the extended X-ray emission for all three sources may originate from low-to-moderate redshift groups or poor clusters. The most conspicuous of these is the apparent clustering of galaxies at $z \approx 0.1$ in the area of CXOECDFS J033320.3–274836, an ≈ 20 arcmin² extended X-ray source. CXOECDFS J033209.6–274242 lies in the ≈ 1 Ms CDF-S and was previously detected as an extended source by G02. Optical spectroscopic follow-up observations using the VLT have shown that this source is associated with a galaxy cluster at $z = 0.73$ (Szokoly et al. 2004). Suggestive evidence for clustering at $z \approx 0.7$ is also observed for CXOECDFS J033257.9–280155; this may be an extension of the large-scale structures observed in the ≈ 1 Ms CDF-S (Gilli et al. 2003, 2005). Under the assumption that these sources are indeed groups or poor clusters at the discussed redshifts, we computed the expected soft-band fluxes and luminosities assuming a Raymond-Smith thermal plasma (Raymond & Smith 1977) with $kT = 1.0$ keV (see Table 8). We find that these sources would have rest-frame 0.5–2.0 keV luminosities of $\approx 1\text{--}5 \times 10^{42}$ erg s⁻¹. Further optical spectroscopic observations and analyses beyond the scope of this paper are required for confirmation of the nature of these sources.

7. Summary

We have presented catalogs and basic analyses of point sources detected in the 250 ks ≈ 0.3 deg² Extended *Chandra* Deep Field-South (E-CDF-S). The survey area consists of four observational fields, of similar exposure, with average on-axis flux limits in the 0.5–2.0 keV and 2–8 keV bandpasses of $\approx 1.1 \times 10^{-16}$ erg cm⁻² s⁻¹ and $\approx 6.7 \times 10^{-16}$ erg cm⁻² s⁻¹, respectively. We have presented two catalogs: a main *Chandra* catalog of 762 sources (589 of these are new), which was generated by running WAVDETECT with a false-positive probability threshold of 1×10^{-6} , and a supplementary catalog of 33 lower-significance (false-positive probability threshold of 1×10^{-5}) X-ray sources with optically bright ($R < 23$) counterparts. The X-ray spectral properties and optical fluxes of sources in our main *Chandra* catalog indicate a variety of source types, most of which are absorbed AGNs that dominate at lower X-ray fluxes. The X-ray and optical properties of sources in the supplementary optically bright *Chandra* catalog are mostly consistent with those expected for starburst and normal galaxies. We have presented basic number-count results for point sources in our main *Chandra* catalog and find overall consistency with number counts derived for the ≈ 1 Ms CDF-S in both the 0.5–2.0 keV and 2–8 keV bandpasses. We have also presented three 0.5–2.0 keV extended sources, which were detected using a conservative detection criterion. These sources are likely associated with groups or poor clusters at $z \approx 0.1\text{--}0.7$ with $L_X \approx 1\text{--}5 \times 10^{42}$ erg s⁻¹.

We thank G. Chartas, P.E. Freeman, A.T. Steffen, and L.K. Townsley for helpful discussions. We thank the anonymous referee for useful comments that improved the manuscript. Support for this work was provided by NASA through *Chandra* Award Number GO4-5157 (BDL, WNB, DPS, RG, AMK, TM) issued by the *Chandra* X-ray Observatory Center, which is operated by the Smithsonian Astrophysical Observatory under NASA contract NAS8-03060. We also acknowledge the financial support of NSF CAREER award

AST-9983783 (BDL, WNB), the Royal Society (DMA), the Chandra Fellowship program (FEB), NSF AST 03-07582 (DPS), NASA LTSA Grant NAG5-10875 (TM), and MIUR COFIN grant 03-02-23 (CV).

REFERENCES

- Alexander, D. M., et al. 2003, *AJ*, 126, 539 (A03)
- Arnouts, S., et al. 2001, *A&A*, 379, 740
- Baganoff, F. K., et al. 2003, *ApJ*, 591, 891
- Barger, A.J., Cowie, L.L., Mushotzky, R.F., Yang, Y., Wang, W.-H., Steffen, A.T., & Capak, P. 2005, *AJ*, 129, 578
- Bauer, F.E., et al. 2002, *AJ*, 123, 1163
- Bauer, F.E., Alexander, D.M., Brandt, W.N., Schneider, D.P., Treister, E., Hornschemeier, A.E., & Garmire, G.P. 2004, *AJ*, 128, 2048
- Bickel, P.J. 1992, in *Statistical Challenges in Modern Astronomy*, eds. Feigelson, E.D., & Babu, G.J. (Springer-Verlag, New York), p. 320
- Boller, Th., Bertoldi, F., Dennefeld, M., & Voges, W. 1998, *A&AS*, 129, 87
- Brandt, W. N., et al. 2001, *AJ*, 122, 2810 (B01)
- Brandt, W.N., & Hasinger, G. 2005, *ARAA*, in press (astro-ph/0501058)
- Broos, P., et al. 2000, *User's Guide for the TARA Package*. The Pennsylvania State University, University Park
- della Ceca, R., Castelli, G., Braitto, V., Cagnoni, I., & Maccacaro, T. 1999, *ApJ*, 524, 674
- Dobrzycki, A., Ebeling, H., Glotfelty, K., Freeman, P., Damiani, F., Elvis, M., & Calderwood, T. 2002, *Chandra Detect 2.2.1 User Guide*. *Chandra X-ray Center*, Cambridge
- Eadie, W.T., Dryard, D., James, F.E., Roos, M., & Sadoulet, B. 1971, *Statistical Methods in Experimental Physics*. North-Holland, Amsterdam
- Ebeling, H. & Wiedenmann, G. 1993, *Phys. Rev. E*, 47, 704
- Feigelson, E.D., Broos, P.S., & Gaffney, J. 2000, *Memo on the Optimal Extraction Radius for ACIS Point Sources*. The Pennsylvania State University, University Park
- Freeman, P.E., Kashyap, V., Rosner, R., & Lamb, D.Q. 2002, *ApJS*, 138, 185
- Garmire, G. P., Bautz, M. W., Ford, P. G., Nousek, J. A., & Ricker, G. R. 2003, *Proc. SPIE*, 4851, 28
- Gawiser, E., et al. 2005, *ApJS*, submitted
- Gendreau, K. C. et al. 1995, *PASJ*, 47, L5

- Gehrels, N. 1986, ApJ, 303, 336
- Giacconi, R., et al. 2002, ApJS, 139, 369 (G02)
- Giavalisco, M., et al. 2004, ApJ, 600, L93
- Gilli, R., et al. 2003, ApJ, 592, 721
- Gilli, R., et al. 2005, A&A, 430, 811
- Harrison, F. A., Eckart, M. E., Mao, P. H., Helfand, D. J., & Stern, D. 2003, ApJ, 596, 944
- Hornschemeier, A.E., et al.2001, ApJ, 554, 742
- Hornschemeier, A.E., et al. 2003, AJ, 126, 575
- Hornschemeier, A. E., et al. 2004, ApJ, 600, L147
- Jerius, D., Donnelly, R.H., Tibbetts, M.S., Edgar, R.J., Gaetz, T.J., Schwartz, D.A., Van Speybroeck, L.P., & Zhao, P. 2000, Proc. SPIE, 4012, 17
- Kraft, R.P., Burrows, D.N. & Nousek, J.A. 1991, ApJ, 374, 344
- Le Fevre, O., et al. 2004, A&A, 428, 1043
- Lonsdale, C.J., et al. 2003, PASP, 115, 897
- Lyons, L. 1991, Data Analysis for Physical Science Students. Cambridge University Press, Cambridge
- Maccacaro, T., Gioia, I.M., Wolter, A., Zamorani, G., & Stocke, J.T. 1988, ApJ, 326, 680
- Markevitch, M. 2001, CXC memo (<http://asc.harvard.edu/cal/>)
- Markevitch, M., et al. 2003, ApJ, 583, 70
- Marshall, F. E., Boldt, E. A., Holt, S. S., Miller, R. B., Mushotzky, R. F., Rose, L. A., Rothschild, R. E., & Serlemitsos, P. J. 1980, ApJ, 235, 4
- Mushotzky, R. F., Cowie, L.L., Barger, A.J., & Arnaud, K.A. 2000, Nature, 404, 459
- Nandra, K., et al. 2005, MNRAS, 356, 568
- Norman, C., et al. 2004, ApJ, 607, 721
- Papovich, C., et al. 2004, ApJS, 154, 70
- Raymond, J. C., & Smith, B. W. 1977, ApJS, 35, 419
- Renzini, A., et al. 2003, In *The Mass of Galaxies at Low and High Redshift*, eds. R. Bender and A. Renzini (New York: Springer), 332

- Richards, E. A., Kellermann, K. I., Fomalont, E. B., Windhorst, R. A., & Partridge, R. B. 1998, *AJ*, 116, 1039
- Rix, H., et al. 2004, *ApJS*, 152, 163
- Rosati, P., et al. 2002, *ApJ*, 566, 667
- Stark, A. A., Gammie, C. F., Wilson, R. W., Bally, J., Linke, R. A., Heiles, C., & Hurwitz, M. 1992, *ApJS*, 79, 77
- Stern, D., et al. 2002, *AJ*, 123, 2223
- Stocke, J.T., Morris, S.L., Gioia, I.M., Maccacaro, T., Schild, R., Wolter, A., Fleming, T.A., & Henry, J.P. 1991, *ApJS*, 76, 813
- Streblyanska, A., Bergeron, J., Brunner, H., Finoguenov, A., Hasinger G., & Mainieri, V. 2004, *Nuc Phys B*, 132, 232
- Szokoly, G., et al. 2004, *ApJS*, 155, 271
- Townsley, L.K., Broos, P.S., Garmire, G.P., & Nousek, J.A. 2000, *ApJ*, 534, L139
- Townsley, L.K., Broos, P.S., Nousek, J.A., & Garmire, G.P. 2002, *Nuclear Instruments and Methods in Physics Research A*, 486, 751
- Tozzi, P., et al. 2001, *ApJ*, 562, 42
- Ueda, Y., Takahashi, T., Ishisaki, Y., Ohashi, T., & Makishima, K. 1999, *ApJ*, 524, L11
- Vanzella, E., et al. 2005, *A&A*, 434, 53
- Vikhlinin, A. 2001, CXC memo (<http://asc.harvard.edu/cal/>)
- Wang, J. X., et al. 2004a, *AJ*, 127, 213
- Wang, J. X., et al. 2004b, *ApJ*, 608, L21
- Wolf, C., et al. 2004, *A&A*, 421, 913

Table 1. Journal of Extended *Chandra* Deep Field-South Observations

Obs. ID	Obs. Start (UT)	Exposure Time (ks) ^a	Aim Point		Roll Angle (°) ^b	Field Number	Pipeline Version
			α_{2000}	δ_{2000}			
5015.....	2004-02-29, 21:21	162.9	03 33 05.61	–27 41 08.84	270.2	1	7.1.1
5016.....	2004-03-03, 12:09	77.2	03 33 05.61	–27 41 08.84	270.2	1	7.2.0
5017.....	2004-05-14, 01:09	155.4	03 31 51.43	–27 41 38.80	181.5	2	7.2.1
5018.....	2004-05-16, 13:44	72.0	03 31 51.43	–27 41 38.80	181.5	2	7.2.1
5019.....	2004-11-17, 14:43	163.1	03 31 49.94	–27 57 14.56	0.2	3	7.3.2
5020.....	2004-11-15, 23:25	77.6	03 31 49.94	–27 57 14.56	0.2	3	7.3.2
5021.....	2004-11-13, 03:26	97.8	03 33 02.93	–27 57 16.08	0.2	4	7.3.2
5022.....	2004-11-15, 00:51	79.1	03 33 02.93	–27 57 16.08	0.2	4	7.3.2
6164.....	2004-11-20, 21:08	69.1	03 33 02.93	–27 57 16.08	0.2	4	7.3.2

^aAll observations were continuous. The short time intervals with bad satellite aspect are negligible and have not been removed.

^bRoll angle describes the orientation of the *Chandra* instruments on the sky (see Figure 2). The angle is between 0–360°, and it increases to the West of North (opposite to the sense of traditional position angle).

Table 2. Main *Chandra* Catalog Source Properties

No.	X-ray Coordinates				Counts					
	α_{2000}	δ_{2000}	Pos Err	Off-Axis	FB	FB Upp Err	FB Low Err	SB	SB Upp Err	SB Low Err
(1)	(2)	(3)	(4)	(5)	(6)	(7)	(9)	(10)	(11)	(12)
1 ...	03 31 11.40	–27 33 38.5	2.6	11.95	29.0	11.7	10.6	20.2	–1	–1
2 ...	03 31 12.99	–27 55 48.2	0.8	8.29	326.8	20.9	19.8	152.1	14.2	13.2
3 ...	03 31 14.09	–28 04 20.3	2.3	10.63	27.1	–1	–1	21.3	7.6	6.4
4 ...	03 31 14.24	–27 47 07.3	0.8	9.87	99.2	13.4	12.3	76.5	10.7	9.7
5 ...	03 31 14.64	–28 01 44.3	0.8	9.00	73.3	11.9	10.8	27.4	7.5	6.3

Note. — Table 2 is presented in its entirety in the electronic edition. An abbreviated version of the table is shown here for guidance as to its form and content. The full table contains 39 columns of information on the 762 X-ray sources.

Table 3. Main *Chandra* Catalog Cross-Field Source Properties

X-ray Coordinates					Counts					
No. (1)	α_{2000} (2)	δ_{2000} (3)	Pos Err (4)	Off-Axis (5)	FB (6)	FB Upp Err (7)	FB Low Err (8)	SB (9)	SB Upp Err (10)	SB Low Err (11)
367 ...	03 32 25.22	–27 42 19.4	0.8	9.02	62.7	11.2	10.1	38.0	8.1	7.1
369 ...	03 32 25.62	–27 43 05.8	0.8	9.06	81.1	12.1	11.0	53.4	9.2	8.1
372 ...	03 32 25.91	–28 00 46.7	1.8	8.90	22.3	8.7	7.6	14.4	–1	–1
373 ...	03 32 26.18	–27 37 12.1	2.0	9.58	35.1	10.3	9.2	22.0	7.3	6.1
375 ...	03 32 26.49	–27 40 35.4	0.7	7.84	295.8	20.1	18.9	244.0	17.7	16.6
376 ...	03 32 26.52	–27 35 02.4	0.9	10.21	95.3	13.8	12.7	72.8	10.9	9.9
377 ...	03 32 26.65	–27 40 14.0	0.8	8.67	185.9	17.1	16.0	110.1	12.9	11.8
379 ...	03 32 27.00	–27 41 05.2	0.7	7.90	1755.3	44.0	43.0	1175.1	36.3	35.3
381 ...	03 32 27.12	–28 01 24.4	0.8	9.21	425.9	23.9	22.7	347.7	20.5	19.5
382 ...	03 32 27.37	–28 05 51.6	0.9	11.94	865.2	33.8	32.7	622.5	27.2	26.1
383 ...	03 32 27.62	–27 41 44.9	0.8	8.02	63.6	11.0	9.8	20.3	6.8	5.7
387 ...	03 32 29.01	–27 57 30.3	0.8	8.63	72.2	11.2	10.1	55.4	9.1	8.0
388 ...	03 32 29.25	–28 01 46.0	2.0	9.79	12.0	9.2	8.1	12.3	–1	–1
753 ...	03 33 38.54	–27 49 42.3	2.4	11.24	28.7	11.3	10.2	19.9	–1	–1

Note. — Basic source properties for the 14 objects detected in more than one observational field. These properties are derived from the observation not included in the main *Chandra* catalog. Columns follow the same format as those presented in Table 2; all 39 columns of this table are available via the electronic version.

Table 4. Summary of *Chandra* Source Detections

Band (keV)	Observational Field	Number of Sources	Detected Counts Per Source			
			Maximum	Minimum	Median	Mean
Full (0.5–8.0)	1	191	2509.4	3.9	43.4	123.2
Soft (0.5–2.0)	1	167	1715.7	3.7	28.4	91.3
Hard (2–8)	1	128	787.7	3.9	29.0	60.8
Full (0.5–8.0)	2	165	2346.5	5.2	37.7	110.2
Soft (0.5–2.0)	2	144	1689.4	4.4	25.5	77.4
Hard (2–8)	2	109	735.2	4.3	25.2	59.2
Full (0.5–8.0)	3	187	1078.3	6.0	39.3	85.4
Soft (0.5–2.0)	3	156	756.6	4.6	24.3	61.1
Hard (2–8)	3	128	324.5	3.7	26.1	45.8
Full (0.5–8.0)	4	160	1771.6	4.2	37.1	115.7
Soft (0.5–2.0)	4	142	1312.0	4.2	25.8	85.0
Hard (2–8)	4	98	514.8	4.7	28.2	60.9
Full (0.5–8.0)	1,2,3,4	689	2509.4	3.9	38.6	104.8
Soft (0.5–2.0)	1,2,3,4	598	1715.7	3.7	25.9	75.7
Hard (2–8)	1,2,3,4	453	787.7	3.7	27.8	55.0

Table 5. Sources Detected In One Band But Not Another

Detection Band (keV)	Nondetection Energy Band		
	Full	Soft	Hard
Full (0.5–8.0)	149	251
Soft (0.5–2.0)	58	...	241
Hard (2–8)	15	96	...

Table 6. Supplementary Optically Bright *Chandra* Catalog

X-ray Coordinates					Counts					
No.	α_{2000}	δ_{2000}	Pos Err	Off-Axis	FB	FB Upp Err	FB Low Err	SB	SB Upp Err	SB Low Err
(1)	(2)	(3)	(4)	(5)	(6)	(7)	(8)	(9)	(10)	(11)
1 ...	03 31 16.20	–27 50 30.9	1.2	10.04	17.9	5.3	4.2	12.3	–1	–1
2 ...	03 31 22.00	–27 36 20.1	1.2	8.41	17.0	5.2	4.1	11.5	–1	–1
3 ...	03 31 28.87	–27 53 29.9	1.2	5.97	12.1	4.6	3.4	9.1	–1	–1
4 ...	03 31 35.14	–27 58 08.6	1.2	3.39	10.0	–1	–1	2.8	2.9	1.6
5 ...	03 31 39.05	–28 02 21.1	1.2	5.65	14.6	–1	–1	1.5	2.5	1.1

Note. — Table 6 is presented in its entirety in the electronic edition. An abbreviated version of the table is shown here for guidance as to its form and content. The full table contains 33 columns of information on the 33 X-ray sources.

Table 7. Background Parameters

Band (keV)	Observational Field	Mean Background		Total Background ^c (10 ⁴ counts)	Count Ratio ^d (background/source)
		(counts pixel ^{–1}) ^a	(counts Ms ^{–1} pixel ^{–1}) ^b		
Full (0.5–8.0).....	1	0.033	0.169	14.6	6.0
Soft (0.5–2.0).....	1	0.009	0.044	3.9	2.5
Hard (2–8).....	1	0.024	0.128	10.8	12.7
Full (0.5–8.0).....	2	0.036	0.192	15.8	8.6
Soft (0.5–2.0).....	2	0.009	0.066	4.1	3.6
Hard (2–8).....	2	0.027	0.143	11.7	16.9
Full (0.5–8.0).....	3	0.037	0.181	16.1	10.1
Soft (0.5–2.0).....	3	0.009	0.046	4.0	4.2
Hard (2–8).....	3	0.027	0.140	12.1	19.5
Full (0.5–8.0).....	4	0.039	0.228	17.4	9.4
Soft (0.5–2.0).....	4	0.010	0.048	4.4	3.6
Hard (2–8).....	4	0.030	0.148	13.1	20.6
Full (0.5–8.0).....	1,2,3,4	0.036	0.192	63.9	8.5
Soft (0.5–2.0).....	1,2,3,4	0.009	0.051	16.3	3.5
Hard (2–8).....	1,2,3,4	0.027	0.140	47.7	17.4

^aThe mean numbers of counts per pixel. These are measured from the masked background images described in § 4.

^bThe mean numbers of counts per pixel divided by the mean effective exposure. These are measured from the exposure maps and masked background images described in § 4.

^cTotal number of background counts.

^dRatio of the total number of background counts to the total number of source counts.

Table 8. Extended-Source Properties

No.	X-ray Coordinates		Region ^a	Angle ^b	SB Counts ^c	<i>S</i> -to- <i>B</i> Ratio ^d	<i>z</i> ^e	SB Flux ^f	L_X^g
	α_{2000}	δ_{2000}							
1	03 32 09.62	–27 42 42.2	100'' × 60''	335°	44.1 ± 16.5	0.22	0.7	2.2	4.8
2	03 32 57.94	–28 01 55.4	90'' × 60''	35°	50.5 ± 16.3	0.28	0.7	1.7	4.1
3	03 33 20.32	–27 48 36.2	380'' × 230''	10°	901.0 ± 60.4	0.34	0.1	27.1	0.7

^aExtraction region given as major axis and minor axis in arcseconds.

^bPosition angle of the extraction region.

^cNet 0.5–2.0 keV background-subtracted source counts. These counts have been measured using the specified extraction regions.

^dRatio of the 0.5–2.0 keV source counts to the total number of expected 0.5–2.0 keV background counts.

^eRedshift of candidate group or poor cluster associated with the extended source. All redshifts were inferred from galaxies with optical spectrophotometric redshifts from the COMBO-17 survey with the exception of source number 1, which was previously identified spectroscopically by Szokoly et al. (2004).

^fIntegrated 0.5–2.0 keV X-ray flux in units of 10^{-15} erg cm⁻² s⁻¹, derived for each source assuming a Raymond-Smith thermal plasma spectral energy distribution with $kT = 1.0$ keV at the given redshift.

^gIntegrated 0.5–2.0 keV X-ray luminosity in units of 10^{42} erg s⁻¹.

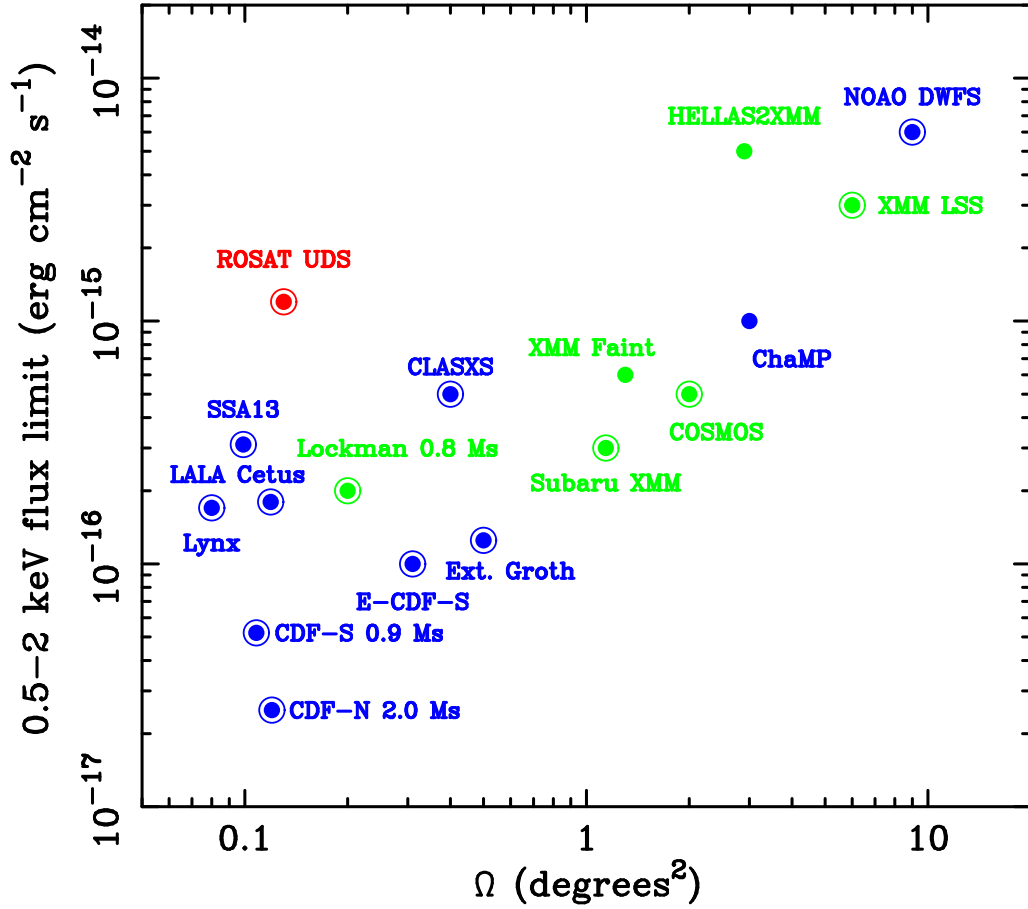


Fig. 1.— Distributions of some well-known extragalactic surveys by *Chandra* (blue), *XMM-Newton* (green), and *ROSAT* (red) in the 0.5–2 keV flux-limit versus solid angle, Ω , plane. Circled dots denote surveys that are contiguous. Each of the surveys shown has a range of flux limits across its solid angle; we have generally shown the most sensitive flux limit. This plot has been adapted from Figure 1 of Brandt & Hasinger (2005) to show the part of parameter space most relevant for the E-CDF-S; see Table 1 of Brandt & Hasinger (2005) for references to descriptions of many of the surveys plotted here.

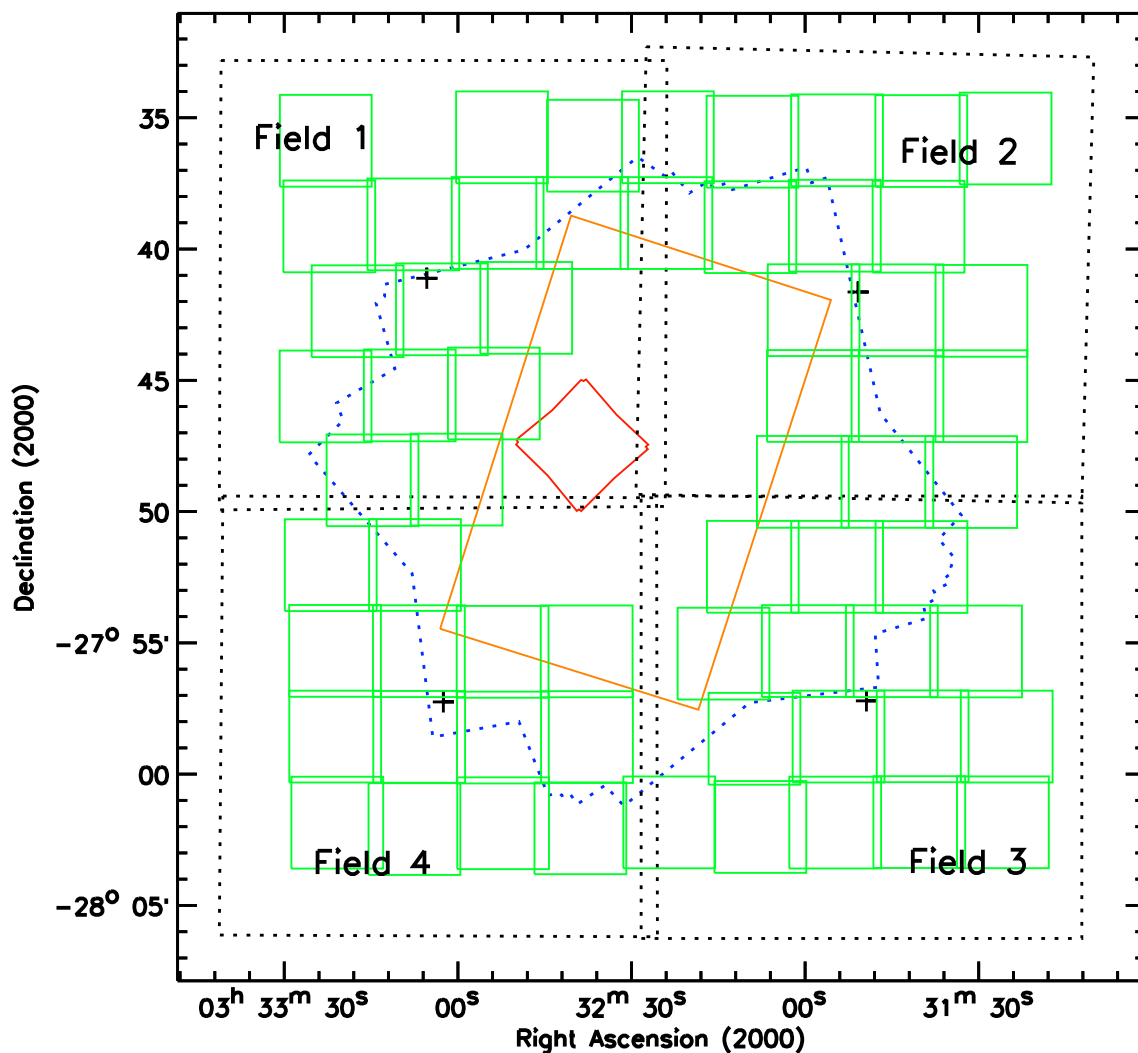


Fig. 2.— Coverage map of the E-CDF-S area showing the various *Chandra* (dashed lines) and *HST* (solid lines) observational regions. The E-CDF-S *Chandra* observational fields are shown as four $16'.9 \times 16'.9$ regions (colored black in the electronic edition) which flank the CDF-S (central polygon [colored blue in the electronic edition]). Each observational field is labeled in text, and the corresponding aim points are indicated as “+” signs within the fields. The *HST* coverage includes the $63, 202'' \times 202''$ square regions (colored green in the electronic edition) from GEMS (Rix et al. 2004), the central rectangle (colored orange in the electronic edition) from GOODS (Giavalisco et al. 2004), and the central $202'' \times 202''$ (colored red in the electronic edition) region of the *Hubble* Ultra Deep Field (UDF; PI: S. Beckwith). The *Spitzer* GOODS coverage coincides with the *HST* GOODS region (central rectangle), and there is a substantial amount of wider field *Spitzer* coverage either executed or approved (see § 1).

This figure is presented in the online edition available at:
<http://www.astro.psu.edu/users/niel/ecdfs/ecdfs-chandra.html>

Fig. 3.— Full-band (0.5–8.0 keV) raw image of the E-CDF-S. Here, all four observational fields have been merged using the CIAO tool `MERGE_ALL`; the *Chandra* aim-points for each field are marked with “+” symbols. Field numbers are printed over each observational field to show their relative locations; note the increase in background where these fields overlap. The CDF-S, GOODS, and UDF regions are marked as per Figure 2.

This figure is presented in the online edition available at:
<http://www.astro.psu.edu/users/niel/ecdfs/ecdfs-chandra.html>

Fig. 4.— Full-band (0.5–8.0 keV) adaptively smoothed and exposure-corrected image of the E-CDF-S. The image was created using the CIAO tool CSMOOTH, applied to the raw-image (presented in Figure 3) at the 2.5σ level. The grayscales are linear. Symbols and regions have the same meaning as those shown in Figure 3.

This figure is presented in the online edition available at:
<http://www.astro.psu.edu/users/niel/ecdfs/ecdfs-chandra.html>

Fig. 5.— Full-band exposure map of the E-CDF-S. The grayscales are linear with the darkest areas corresponding to the highest effective exposure times (the high effective exposure times between fields is due to overlap of observations). Note the chip gaps in white running between the four ACIS-I CCDs. Symbols and regions have the same meaning as those shown in Figure 3.

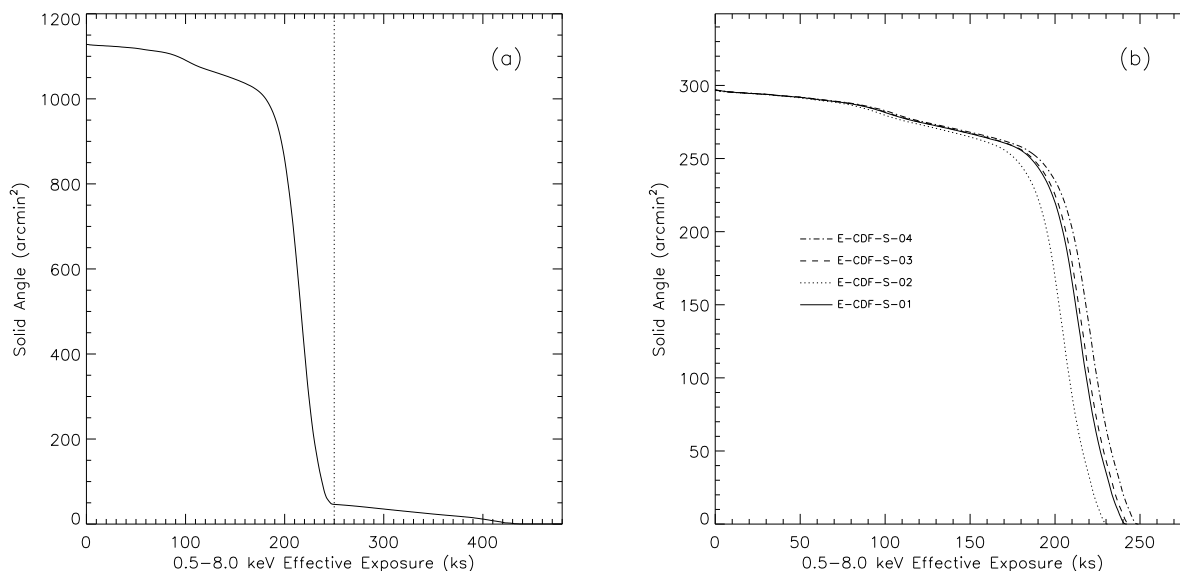


Fig. 6.— **(a)** Amount of survey solid angle having at least a given amount of effective exposure in the full-band exposure map for the entire E-CDF-S. The “tail” with exposure times > 250 ks (right of the vertical line) corresponds to regions where observational fields overlap (see Figure 5). **(b)** Amount of solid angle having at least a given amount of effective full-band exposure for each of the four fields.

This figure is presented in the online edition available at:
<http://www.astro.psu.edu/users/niel/ecdfs/ecdfs-chandra.html>

Fig. 7.— *Chandra* “false-color” image of the E-CDF-S. This image has been constructed from the 0.5–2.0 keV (red), 2–4 keV (green), and 4–8 keV (blue) exposure-corrected adaptively smoothed images discussed in § 3.1.

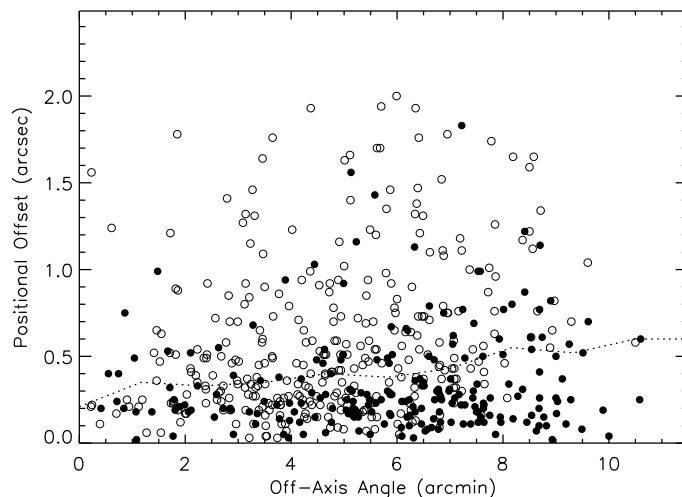


Fig. 8.— Positional offset vs. off-axis angle (computed in each observational field) for sources in the main *Chandra* catalog that were matched to optical sources from the WFI *R*-band image to within $2''5$. Open circles are *Chandra* sources with < 50 full-band counts, and filled circles are *Chandra* sources with ≥ 50 full-band counts. The dotted curve shows the running median for all sources. These data were used to determine the positional uncertainties of the *Chandra* sources; see § 3.3.1.

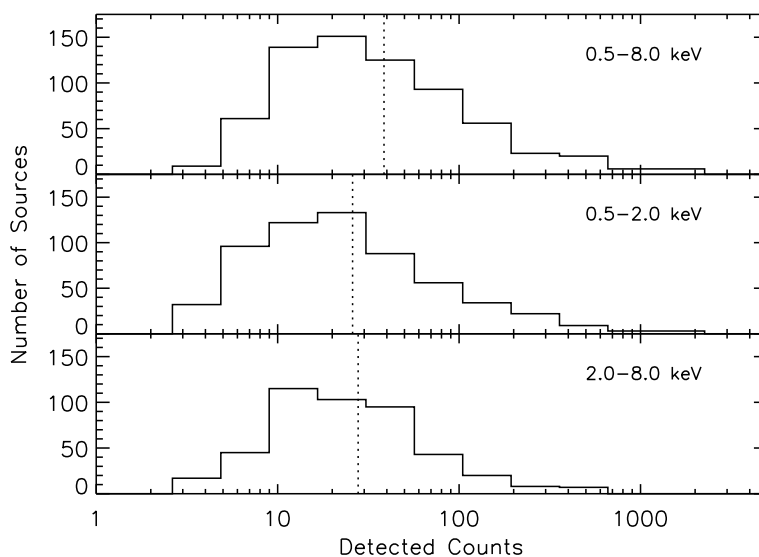


Fig. 9.— Histograms showing the distributions of detected source counts for sources in the main *Chandra* catalog in the full (*top*), soft (*middle*), and hard (*bottom*) bands. Sources with upper limits have not been included in this plot. The vertical dotted lines indicate median numbers of counts (see Table 4).

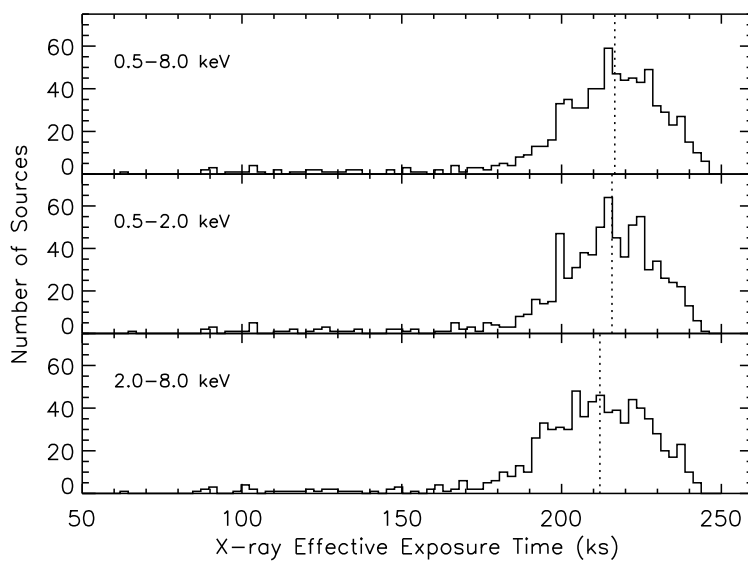


Fig. 10.— Histograms showing the distributions of effective exposure time for the sources in the main *Chandra* catalog in the full (*top*), soft (*middle*), and hard (*bottom*) bands. The vertical dotted lines indicate the median effective exposure times of 217, 216, 212 ks for the full, soft, and hard bands, respectively.

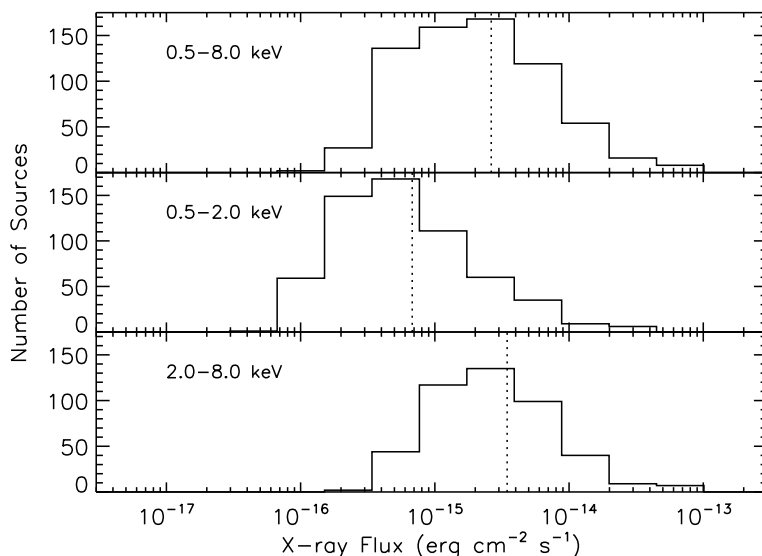


Fig. 11.— Histograms showing the distributions of X-ray fluxes for sources in the main *Chandra* catalog in the full (*top*), soft (*middle*), and hard (*bottom*) bands. Sources with upper limits have not been included in this plot. The vertical dotted lines indicate the median fluxes of 26.3 , 6.8 , and 34.6×10^{-16} erg cm $^{-2}$ s $^{-1}$ for the full, soft, and hard bands, respectively.

This figure is presented in the online edition available at:

<http://www.astro.psu.edu/users/niel/ecdfs/ecdfs-chandra.html>

Fig. 12.— WFI *R*-band postage-stamp images for the sources in the main *Chandra* catalog with full-band adaptively smoothed X-ray contours overlaid. The contours are logarithmic in scale and range from ≈ 0.03 – 30% of the maximum pixel value. Note that for sources with few full-band counts, CSMOOTH has suppressed the observable emission in the adaptively smoothed images and therefore no X-ray contours are observed for these sources. The label at the top of each image gives the source name, which is composed of the source coordinates, while numbers at the bottom left and right hand corners correspond to the source number (see column 1 of Table 1) and full-band source counts, respectively. Each image is $\approx 24''.6$ on a side, and the source of interest is always located at the center of the image. Only one of the thirteen pages of cutouts is included here; all thirteen pages are available at the E-CDF-S website (<http://www.astro.psu.edu/users/niel/ecdfs/ecdfs-chandra.html>).

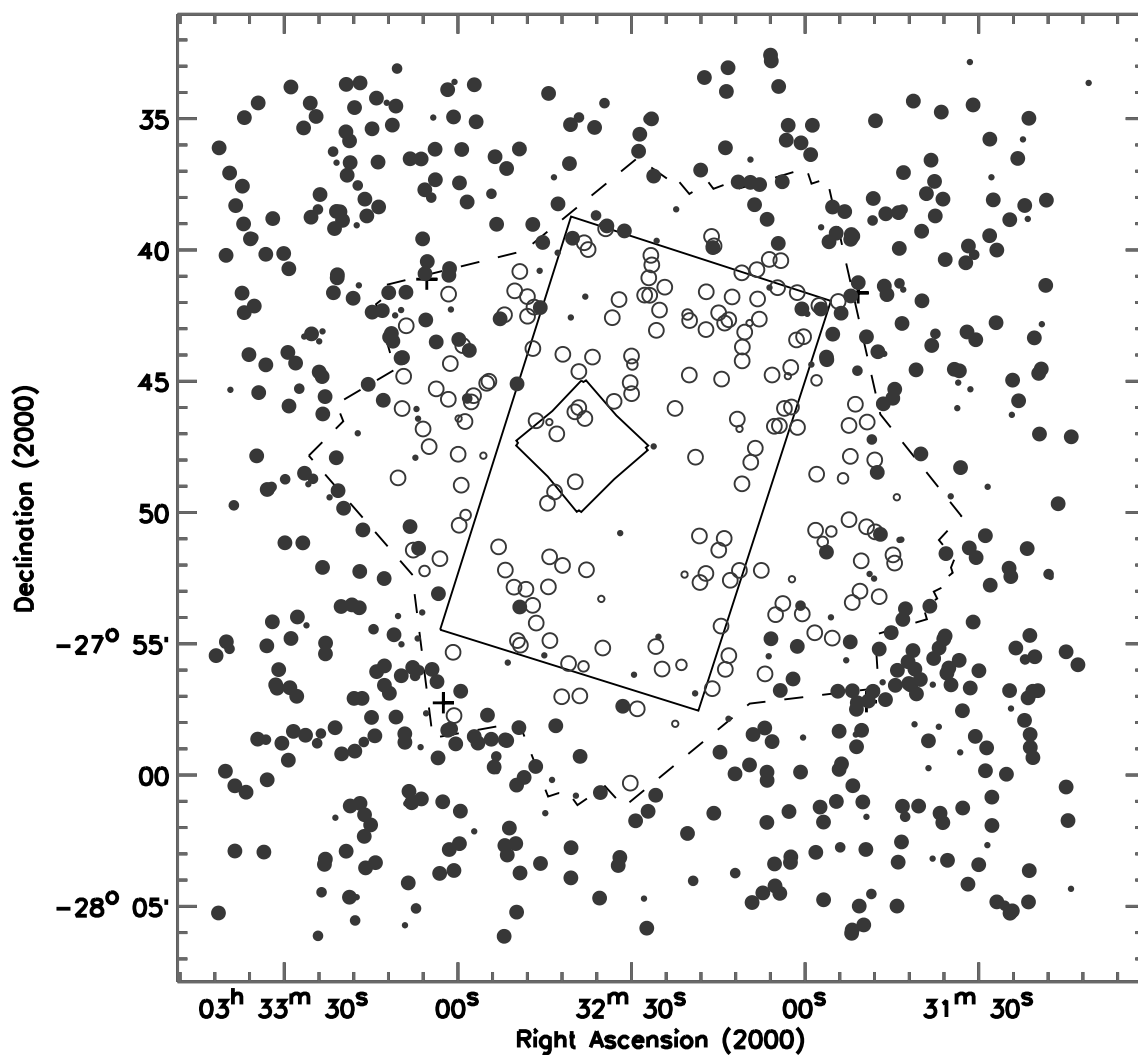


Fig. 13.— Positions of the sources in the main *Chandra* catalog. The regions have the same meaning as those given in Figure 3. New X-ray sources are shown here as filled circles while sources that were previously detected in the ≈ 1 Ms CDF-S are shown as open circles. Large, medium, and small circles correspond to sources with WAVDETECT false-positive probability $\leq 1 \times 10^{-8}$, $\leq 1 \times 10^{-7}$, and $\leq 1 \times 10^{-6}$, respectively.

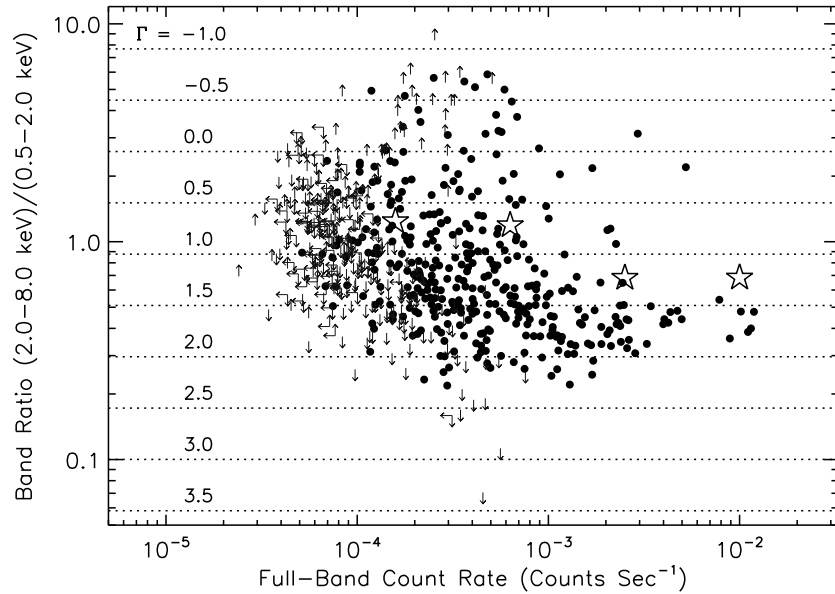


Fig. 14.— Band ratio as a function of full-band count rate for the sources in the main *Chandra* catalog. Small solid dots show sources detected in both the soft and hard bands. Plain arrows show sources detected in only one of these two bands with the arrows indicating upper and lower limits; sources detected in only the full band cannot be plotted. The open stars show average band ratios as a function of full-band count rate. Horizontal dotted lines are labeled with the photon indices that correspond to a given band ratio assuming only Galactic absorption (these were determined using the CXC’s Portable, Interactive, Multi-Mission Simulator; PIMMS).

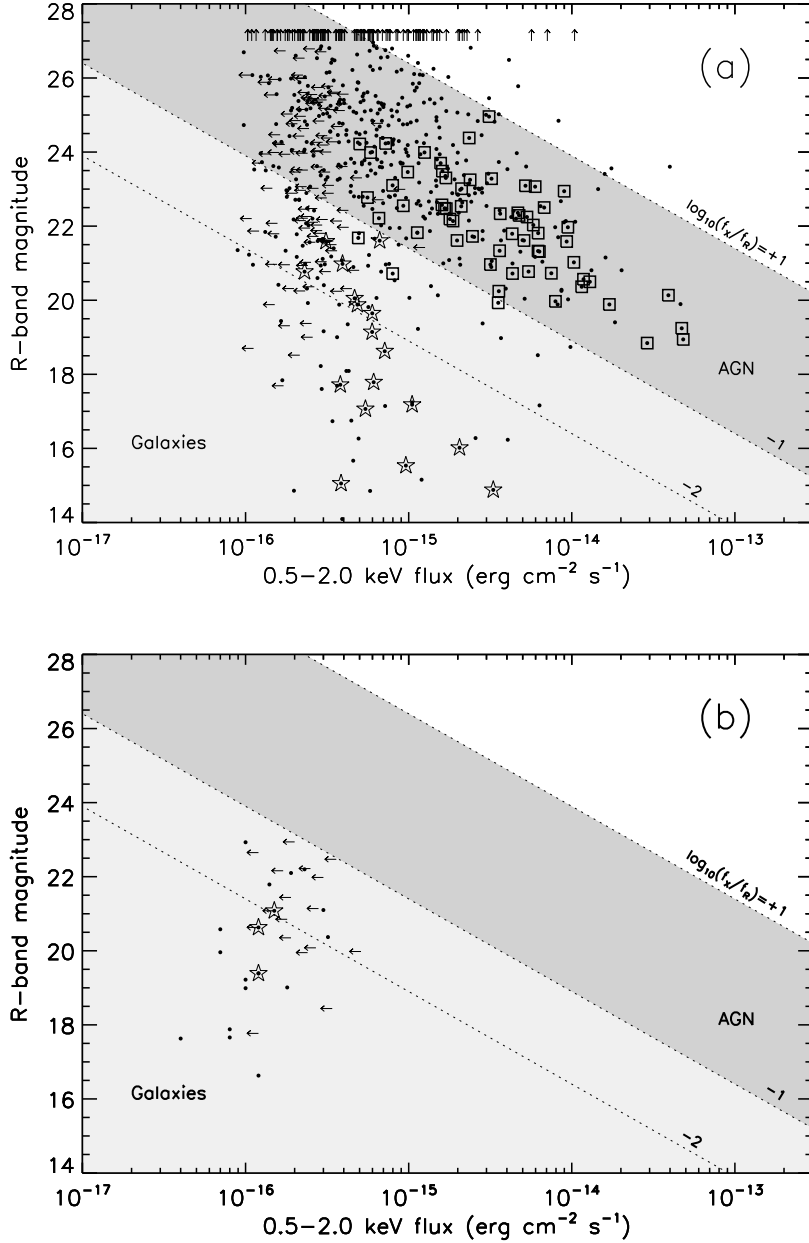


Fig. 15.— **(a)** WFI *R*-band magnitude versus soft-band flux for sources in the main *Chandra* catalog. Open-star symbols indicate Galactic stars identified using the optical spectrophotometric COMBO-17 survey (Wolf et al. 2004). Diagonal lines indicate constant flux ratios. Sources that were not detected in the soft band that were detected in at least one of the full and hard bands are plotted here as upper limits. The shaded regions show the approximate flux ratios for AGNs and galaxies (dark and light, respectively); the sixty-one AGNs with reliable COMBO-17 identifications are plotted as squares. **(b)** WFI *R*-band magnitude versus soft-band flux for sources in the optically bright supplementary catalog. Note that many of these sources have X-ray-to-optical flux ratios expected for normal and starburst galaxies.

This figure is presented in the online edition available at:
<http://www.astro.psu.edu/users/niel/ecdfs/ecdfs-chandra.html>

Fig. 16.— Full-band background map of the E-CDF-S. This background map has been created following § 4. Symbols and regions have the same meaning as those given in Figure 3.

This figure is presented in the online edition available at:
<http://www.astro.psu.edu/users/niel/ecdfs/ecdfs-chandra.html>

Fig. 17.— Full-band sensitivity map of the E-CDF-S. This sensitivity map has been created following § 4. Symbols and regions have the same meaning as those given in Figure 3. Black, dark gray, light gray, and white areas correspond to flux-limits of $<3 \times 10^{-16} \text{ erg cm}^{-2} \text{ s}^{-1}$, $3\text{--}7.8 \times 10^{-16} \text{ erg cm}^{-2} \text{ s}^{-1}$, $7.8\text{--}20 \times 10^{-16} \text{ erg cm}^{-2} \text{ s}^{-1}$, and $> 20 \times 10^{-16} \text{ erg cm}^{-2} \text{ s}^{-1}$, respectively. The central dashed circle ($\approx 6'$ radius) shows the approximate region of the $\approx 1 \text{ Ms}$ CDF-S where the full band flux-limit is $<3 \times 10^{-16} \text{ erg cm}^{-2} \text{ s}^{-1}$. Note the most sensitive regions of the E-CDF-S exposure lie just outside the $\approx 1 \text{ Ms}$ CDF-S exposure.

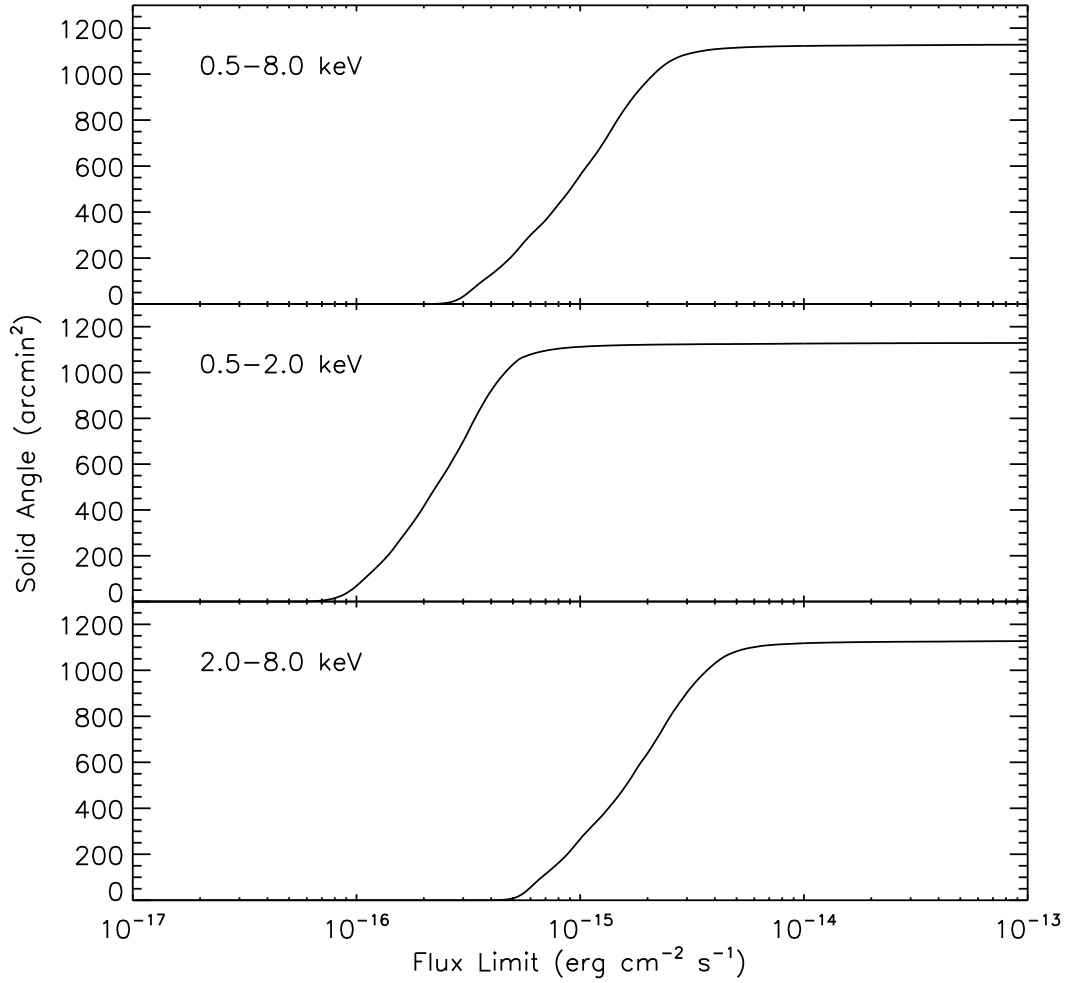


Fig. 18.— Solid angle vs. flux limit for the full (*top*), soft (*middle*), and hard (*bottom*) bands, determined following § 4. The average flux limits (averaged over the four observational fields) at the aim points are 3.5×10^{-16} erg cm⁻² s⁻¹ (full-band), 1.1×10^{-16} erg cm⁻² s⁻¹ (soft-band), and 6.7×10^{-16} erg cm⁻² s⁻¹ (hard-band).

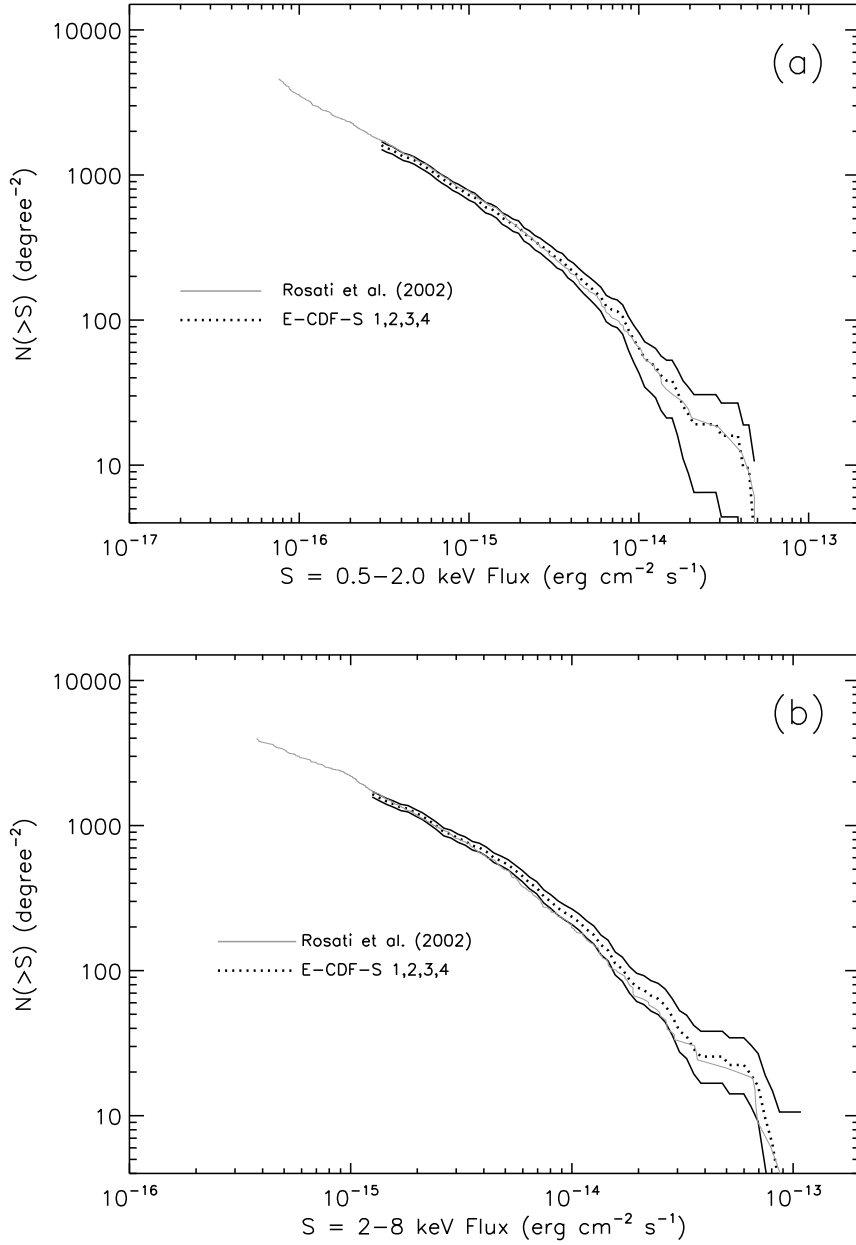


Fig. 19.— Number of sources, $N(> S)$, brighter than a given flux, S , for the **(a)** soft band and **(b)** hard band. In both figures, data from our main *Chandra* catalog are plotted as black dotted curves with the 1σ errors (computed following Gehrels et al. 1986) plotted as black solid curves. In both figures, the observed number counts for the ≈ 1 Ms CDF-S (adapted from Rosati et al. 2002) are plotted in gray for comparison.

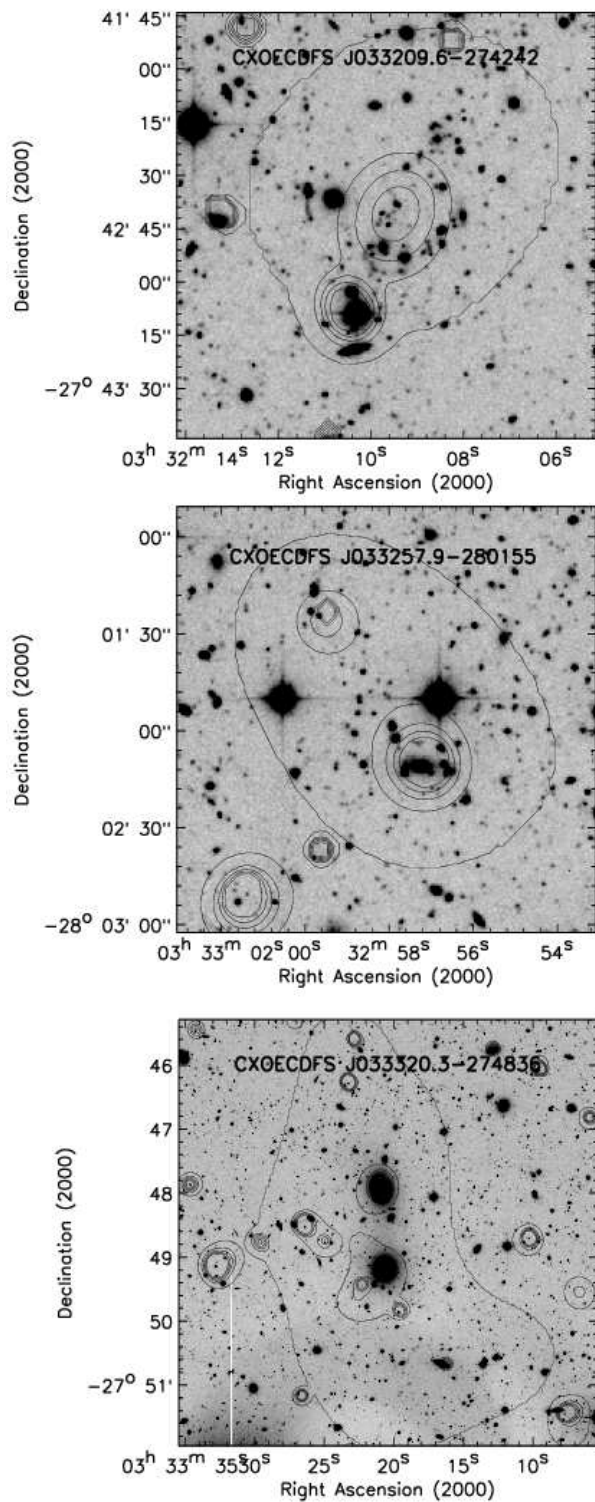


Fig. 20.— WFI *R*-band images with adaptively smoothed 0.5–2.0 keV X-ray contours of the spatially extended X-ray sources CXOECDFS J033209.6–274242, CXOECDFS J033257.9–280155, and CXOECDFS J033320.3–274836. Contours are at 10%, 30%, 50%, 70%, and 90% of the maximum pixel value. Note that each panel has a different size.